JGR Solid Earth

RESEARCH ARTICLE
10.1029/2018JB017277

Special Section:
Magnetism in the Geosciences - Advances and Perspectives

Key Points:
- Inputs of sulfate and methane-rich pore fluids produce repeated episodes of greigite authigenesis and conversion to pyrite
- Slow background pyritization converts greigite to pyrite at a log-linear rate with burial depth and age
- Neither background nor local fluid-driven magnetic mineral diagenesis completely obliterates the magnetic polarity stratigraphy

Supporting Information:
- Supporting Information S1

Correspondence to:
R. J. Musgrave,
robert.musgrave@planning.nsw.gov.au

Citation:
Musgrave, R. J., Kars, M., & Vega, M. E. (2019). Progressive and punctuated magnetic mineral diagenesis: The rock magnetic record of multiple fluid inputs and progressive pyritization in a volcano-bounded basin, IODP Site U1437, Izu rear arc. *Journal of Geophysical Research: Solid Earth*, *124*, 5357–5378. https://doi.org/10.1029/2018JB017277

Received 28 DEC 2018
Accepted 24 MAY 2019
Accepted article online 4 JUN 2019
Published online 26 JUN 2019

Progressive and Punctuated Magnetic Mineral Diagenesis: The Rock Magnetic Record of Multiple Fluid Inputs and Progressive Pyritization in a Volcano-Bounded Basin, IODP Site U1437, Izu Rear Arc

Robert J. Musgrave[1,2,3], Myriam Kars[4], and Marta E. Vega[1]

[1]Geological Survey of New South Wales, NSW Department of Planning and Environment, Maitland, New South Wales, Australia, [2]School of Geosciences, University of Sydney, Sydney, New South Wales, Australia, [3]School of Environmental and Life Sciences, The University of Newcastle, Callaghan, New South Wales, Australia, [4]Center for Advanced Marine Core Research, Kochi University, Monobe, Japan

Abstract International Ocean Discovery Program (IODP) Site U1437 recovered an 1,800-m-long sediment sequence in a volcano-bounded basin on the Izu rear arc. Pore fluid studies revealed a pattern of repeated fluid inputs, fluid diffusion, and methane and ethane accumulations, which represent "fluid anomalies" that disturb the fluid profiles. First-order reversal curve analysis, magnetic hysteresis, saturation isothermal remanent magnetization, and low-temperature remanence cycling reveal a detrital input dominated by vortex-state and multidomain magnetite, which passes through an initial stage of partial magnetite dissolution and greigite authigenesis in the upper few tens of meters. Progressive magnetic mineral diagenesis comprises the continued loss of fine-grained magnetite and gradual pyritization of greigite and produces a background logarithmic decrease in saturation isothermal remanent magnetization normalized by magnetic susceptibility. This process implies a continuing slow supply of S^{2-} to depths >1,500 m. Thermally driven diagenesis, which would cause extensive loss of greigite at these depths, does not appear to be significant here. Multidomain magnetite grains dominate the magnetic mineralogy in the deepest part of the sequence, but some single-domain magnetite survives as inclusions in silicates. Fluid anomalies representing sulfate influx drive locally renewed greigite authigenesis, as do methane and ethane accumulations. In some cases, where methane is accompanied by H_2S ("sour gas"), fine-grained greigite is converted to pyrite. We term these multiple episodes of enhanced magnetic mineral alteration "punctuated magnetic mineral diagenesis." Despite both progressive and punctuated magnetic mineral diagenesis, enough depositional remanence survives to allow recognition of the magnetostratigraphy to 1,320 m below seafloor.

1. Introduction

Magnetic mineral diagenesis in marine sediments is a cumulative process that modifies the detrital load of magnetic minerals by dissolution of existing minerals and authigenesis of new magnetic phases. Roberts (2015) provided an extensive overview of existing studies, which have typically examined the process from one of three viewpoints: early magnetic mineral diagenesis, deep progressive magnetic mineral diagenesis, and isolated intervals of late magnetic mineral diagenesis, as outlined briefly below.

Early magnetic mineral diagenesis commences in the first few meters below the seafloor, and proceeds through a series of redox zones, culminating in the transition from the sulfidic zone, where sulfate reduction yields H_2S, to the methanic zone, in which methanogenesis dominates (Canfield & Thamdrup, 2009). Where sufficient methane is available, anaerobic oxidation of methane (AOM) results in the near-complete reduction of sulfate at the sulfate-methane transition (SMT; Goldhaber, 2003), liberating sulfide which diffuses both up and down, dissolving detrital magnetite and producing iron sulfides, including the ferrimagnet greigite, and culminating in pyrite formation (Garming et al., 2005; Jørgensen et al., 2004; Kasten et al., 1998; Neretin et al., 2004). Greigite can survive if the pyritization process is left incomplete through limitations in the supply of sulfate relative to Fe^{2+} (Horng & Chen, 2006). Early magnetic mineral diagenesis is modulated by nonsteady state input of organic material and iron-bearing minerals, which often reflect climate signals (e.g., Dekkers et al., 1994; Kars et al., 2017; Larrasoaña et al., 2003; Tarduno, 1992).

Other studies have considered progressive magnetic mineralogical changes, extending over hundreds of meters of sequence and driven by thermal maturation during burial (e.g., Aubourg et al., 2012; Kars et al., 2012). Such processes are usually seen as a unidirectional succession of changing magnetic mineralogy, with more thermally mature phases sequentially replacing those originating at lower burial temperatures, for example, in the series from greigite to magnetite to pyrrhotite (Kars et al., 2014).

Most studies of late diagenesis have focused on localized, episodic events driven by incursions of fluids bearing sulfate or sulfide (Roberts & Weaver, 2005; Weaver et al., 2002), or the presence of hydrocarbons as fluids or clathrates (Housen & Musgrave, 1996; Larrasoaña et al., 2007; Musgrave et al., 1995; Reynolds et al., 1994). Both greigite and pyrrhotite have been identified as products of fluid-driven late diagenetic events (e.g., Jiang et al., 2001; Larrasoaña et al., 2007; Weaver et al., 2002). Fluids responsible for late diagenesis are likely to have migrated via permeable zones or faults (e.g., Musgrave et al., 1995).

International Ocean Discovery Program (IODP) Site U1437 offers an opportunity to examine all three of these diagenetic systems, in a setting that offers several advantages (Busby et al., 2017; Tamura et al., 2015). Site U1437 recovered sediment cores over a long interval extending from the seafloor to 1,800 meters below seafloor (mbsf). The recovered sequence is lithologically relatively uniform down to 1,320 mbsf, which reduces the influence of changes in detrital inputs. Heat flow at the site is high (88.2 mW/m^2), and the near-seafloor geothermal gradient of 83 °C/km projects to a temperature of 150 °C near the base of the cored sequence, which allows a test of the greigite to magnetite burial diagenesis transition described by Aubourg et al. (2012). Fluid transport into the section, and vertical fluid diffusion within the section, are well characterized by pore water analyses that extended to 700 mbsf, and headspace gas analysis reveals intervals of methane and ethane accumulation from about 750 to 1,450 mbsf. The stratigraphic age through most of the section is well constrained by a combination of magnetostratigraphy and biostratigraphy, and a detailed age model combining biostratigraphic, magnetostratigraphic, and oxygen isotope data for the last 1 Myr has been produced (Mleneck-Vautravers, 2018). Climate controls on nonsteady state magnetic diagenesis from the uppermost 120 m of the sedimentary record at Site U1437 have already been reported (Kars et al., 2017), as has a detailed description of the late magnetic mineral diagenesis associated with a deep methane-rich zone between 850 and 1,000 mbsf (Kars et al., 2018), while the challenges presented in the recognition of magnetostratigraphy at Site U1437 have been presented by Musgrave and Kars (2016).

Our aims in this study are to (i) identify the effects of deep burial and elevated temperatures over the entire 1,800 m cored at Site U1437, testing the extent to which thermal maturation and burial diagenesis have resulted in replacement of the depositional magnetic mineralogy ("progressive magnetic mineral diagenesis"), and the degree to which this is perturbed by the transition to coarser-grained lithologies in the deeper part of the sequence; (ii) examine the impact on the magnetic mineralogy of the complex pattern of multiple fluid inputs revealed by pore fluid geochemistry ("punctuated magnetic mineral diagenesis"); and (iii) determine the extent to which these two processes combined degrade the paleomagnetic record.

2. Background

2.1. U1437 Setting, Stratigraphy, Age, and Geothermal Gradient

Site U1437 (Figure 1) was drilled during IODP Expedition 350 in a volcano-sedimentary basin within the Izu-Bonin rear arc, about 300 km south of Japan (Busby et al., 2017; Tamura et al., 2015). The water depth at the site is 2,116 m. Coring extended to 439.1 mbsf in Hole U1437B and from 427.2 mbsf to 1,104.6 mbsf in Hole U1437D. Poor recovery and difficult drilling conditions near the bottom of Hole U1437D prompted abandonment of this hole and drilling of Hole U1437E. Coring in this last hole commenced at 1,104.0 mbsf and continued to 1,806.5 mbsf. Tuffaceous mud and mudstone with intercalated ashes and volcaniclastics characterize the uppermost 1,320 m, comprising Lithological Units I through V, with only two comparatively short intervals (Units II and IV) in which fine volcaniclastics dominate. Locally derived volcanic components generally make up 70–100% of the mud fraction, although this drops to 20–50% in intervals deposited during Pleistocene glacials in the upper part of Unit I, where continentally derived hemipelagic muds dominate (Gill et al., 2018; Kars et al., 2017). Unit VI, from 1,320 to 1,460 mbsf, exhibits a coarser volcaniclastic input and a reduced mudstone component than the overlying mud-dominated lithology of Units I through V. Mudstone is absent from the underlying Unit VII, which extends to the bottom of hole. Unit VII

10.1029/2018JB017277

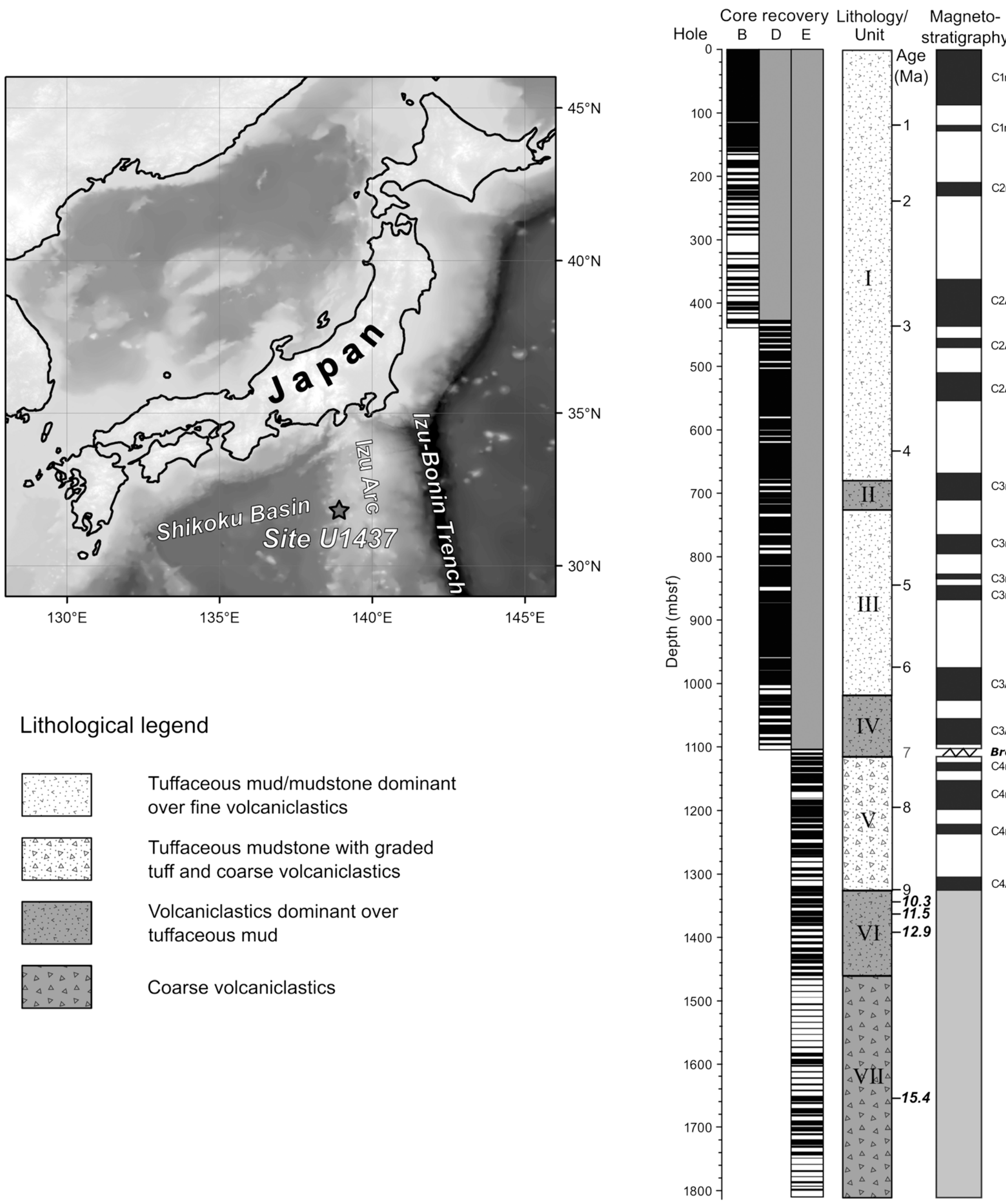

Figure 1. Location, core recovery, stratigraphy, age model, and magnetostratigraphy of Site U1437 (from Tamura et al., 2015). Core recovery columns: black = recovered interval, white = unrecovered interval, gray = drilled without coring. Ages in normal font are from the shipboard age model, based on combined magnetostratigraphy and biostratigraphy: dates in Units VI and VII, marked by bold italics, are postcruise ^{40}Ar-^{39}Ar and zircon U-Pb ages. The break in the magnetostratigraphy column indicates missing section between Holes U1437D and U1437E.

is dominated by lapilli tuff and lapillistone and incorporates coarser volcanic breccia extending up to pebble and cobble size.

Calcareous nannofossils and foraminifers define a series of biostratigraphic datums that extend from the seafloor to 867 mbsf, with the oldest datum at 5.28 Ma (Tamura et al., 2015). Magnetic reversal datums agree closely with biostratigraphic ages and extend the age record to 1,303 mbsf, near the base of the mudstone-dominated sequence where the oldest polarity datum recognized was the top of Chron C4An (8.77 Ma). To our knowledge, this is the longest continuous magnetic polarity stratigraphy ever determined from scientific ocean drilling. Although polarity could be determined from some samples within Units VI and VII, the record was not continuous enough to define a magnetostratigraphy in these units. Sedimentation rates in Units I through V range from 98 to 260 m/My; an apparent loss of stratigraphic section at about 1,100

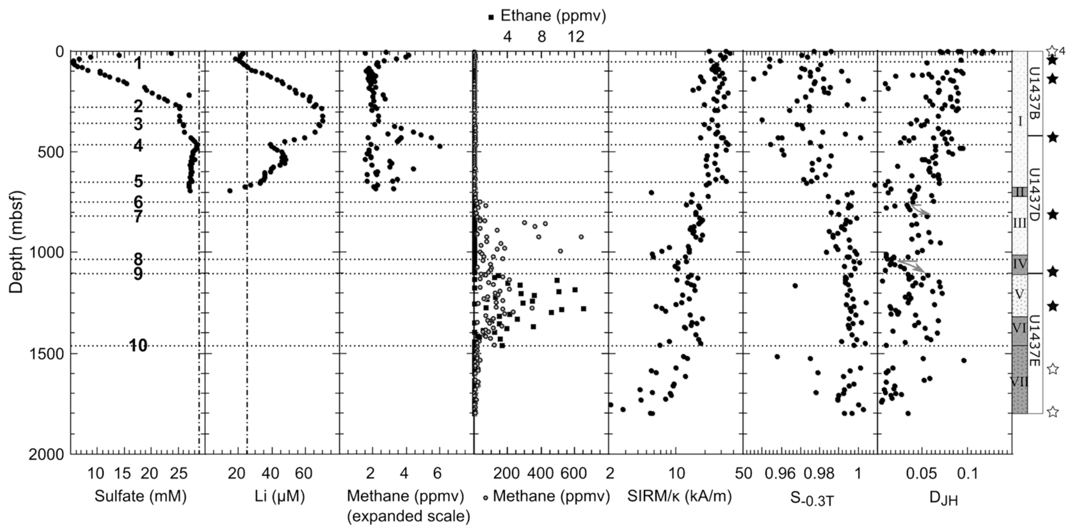

Figure 2. Profiles of fluid geochemistry (selected interstitial water solute and headspace gas hydrocarbon content) and rock magnetic indices SIRM/κ (saturation isothermal remanence normalized by magnetic susceptibility), $S_{-0.3T}$ (a measure of the relative proportion of low-coercivity minerals; Bloemendal et al., 1992), and D_{JH} (an index based on magnetic hysteresis that increases in response to increases in concentration of magnetic sulfides; Housen & Musgrave, 1996). Side column shows stratigraphic column and the extent of coring in the three holes. Stars indicate location of samples subjected to first-order reversal curve (FORC) analysis: solid stars had additional low-temperature remanence studies. Fluid samples were collected and analyzed immediately after sampling onboard ship; methods and results are given in Tamura et al. (2015). Interstitial water sampling was discontinued below 700 mbsf due to increasing lithification. Dashed horizontal lines mark interpreted fluid anomalies, with their numbers. Sea water average compositions are indicated by dash-dotted lines. Gray arrows on D_{JH} plot indicate "D_{JH} notches."

mbsf, between the bottom of Hole U1437D and the top of core recovery in Hole U1437E, is interpreted as due to a normal fault. Postcruise ^{40}Ar-^{39}Ar and zircon U-Pb dating support the shipboard biostratigraphy and magnetostratigraphy and extend the age record into Unit VII, with a U-Pb date of 15.4 ± 1.0 Ma at 1,390 mbsf (Schmitt et al., 2017).

Magnetostratigraphic interpretation is made difficult by intervals in which the dominant remanence carrier appears to be diagenetic greigite, which leads to a secondary remanence acquisition that is expressed as anomalous polarity artifacts termed "ghost polarity intervals" by Musgrave and Kars (2016); these occur at intervals through Unit I and appear to result from diagenetic growth of greigite lagging deposition by up to about 20 m. Fine black grains occur in association with glauconite in bioturbated mud throughout Units I and II but diminish in Unit III (Tamura et al., 2015). Similar clusters of fine black grains have been identified as greigite in studies of reduced continental margin sediments (Jiang et al., 2001; Larrasoaña et al., 2007; Shipboard Scientific Party, 1994; van Dongen et al., 2007).

Site U1437 lies in a basin between the Enpo and Manji rear arc volcanic chains (Busby et al., 2017). This setting has a relatively high geothermal gradient, determined to be 83 °C/km within the upper 60 mbsf. This projects to a temperature of 50 °C at about 570 mbsf, the temperature threshold for neoformation of superparamagnetic (SP) magnetite in claystone observed in experimental studies by Kars et al. (2012). Further projection of the shallow geotherm to the bottom of Hole U1437E predicts a temperature of ~150 °C, where the beginning of neoformation of pyrrhotite in claystone has been invoked (Aubourg & Pozzi, 2010; Kars et al., 2014). However, higher thermal conductivity in the sediments below 700 mbsf (Tamura et al., 2015), and the likelihood that heat input and transport may have been influenced by advective fluid transport, suggests that the geothermal gradient in the lower part of the cored sequence may be lower.

2.2. Fluid Geochemistry and Fluid Migration at Site U1437

What sets Site U1437 aside from other marine sediment sequences which have been the subject of magnetic diagenesis studies (e.g., Channell & Hawthorne, 1990; Garming et al., 2005; Kawamura et al., 2012; Musgrave et al., 1993) is the complexity of its pore fluid profile (Figure 2 and supporting information Figure S1). Interstitial water profiles of sulfate and of Li and other cations show local peaks that were interpreted as evidence for local influx of fluid transported laterally along fracture systems or horizons of enhanced permeability (Tamura et al., 2015). These fluid inputs are either currently active or recent enough to have preserved a diffusion profile. Headspace gas profiles provide additional evidence of fluid transport below the depth at which recovery of interstitial water became impracticable (700 mbsf). Methane, which is present in markedly higher concentrations in the interval from 750 to 1,035 mbsf, may have been locally sourced, but the correlation between total organic carbon contents and gas concentrations is poor (Kars et al., 2018), favoring gas migration. Ethane appeared above detection limits for the first time in the first core below an interpreted fault at the break between the bottom of Hole U1437D and the beginning of coring at the same subbottom depth in Hole U1437E (Musgrave & Kars, 2016; Tamura et al., 2015). Contrasting ethane abundance in the hanging and footwalls of this fault are consistent with gas migration.

We have built on the shipboard interpretation of fluid transport by defining a series of fluid anomalies, where concentration peaks and troughs appear to mark intervals of fluid inflow or other departures from simple sea water diffusion profiles. In downhole sequence, these anomalies are as follows:

1. fluid anomaly 1 (50 mbsf), defined by the minimum sulfate concentration which marks the point where sulfate diffusing from the seafloor toward the sulfate reduction zone (Canfield & Thamdrup, 2009; Jørgensen & Kasten, 2006) meets a second, inverted diffusion profile from sulfate influx deeper in the sequence;
2. fluid anomaly 2 (270 mbsf), where there is a sharp inflection in the sulfate curve marking the top of a diffusion profile and which also defines the top of a broad peak in Li;
3. fluid anomaly 3 (360 mbsf), defined by the base of the Li peak, the top of another sulfate diffusion profile, and the top of an interval of downhole increase in methane;
4. fluid anomaly 4 (460 mbsf), where sulfate reaches its highest concentration, equal to that of seawater, the Li profile is marked by a local minimum, and methane reaches a local maximum before sharply decreasing downhole;
5. fluid anomaly 5 (650 mbsf), an inflection in the Li profile below which Li concentrations decrease rapidly with depth and a small offset in the sulfate profile;
6. fluid anomaly 6 (750 mbsf), where methane exceeds 20 ppmv for the first time, representing the top of the first methane-rich zone;
7. fluid anomaly 7 (830 mbsf), the top of the zone of maximum methane concentration, characterized by methane concentrations in many samples above 200 ppmv;
8. fluid anomaly 8 (1035 mbsf), the base of the maximum methane zone;
9. fluid anomaly 9 (1104 mbsf, corresponding to the interpreted fault at the coring break between Holes U1437D and U1437E), marked by the first appearance of ethane above detection limits and a return to methane concentrations above 100 ppmv;
10. fluid anomaly 10 (1460 mbsf), below which ethane concentrations drop below detection limits and methane also substantially decreases.

Fluid anomaly 10 is the only fluid marker that closely corresponds to a break between lithostratigraphic units (Units VI and VII).

3. Methods

Samples were taken as 8-cm^3 cubes at an interval of approximately one sample per 10 m, selected from mud or mudstone intervals in Units I through VI and from fine-grained volcaniclastic layers in Unit VII. Samples remained damp and were kept in a freezer for most of the period between sampling from the core and measurement, to minimize greigite oxidation. Isothermal remanent magnetization (IRM) studies were conducted on a subset of 49 samples on board the R/V *JOIDES Resolution* (JR), and on a further 88 samples in the PALM laboratory at the University of Newcastle, Australia. IRM was imparted using similar ASC IM-10 pulse magnetizers in both laboratories and was measured on AGICO JR-6A (JR laboratory) or Molspin (PALM laboratory) spinner magnetometers. IRM at 1.0 T, which is considered to represent saturation IRM (SIRM), was imparted along the $+z$ axis. SIRM ranged from 4.4 A/m to 237.6 A/m. Nominal noise levels were 0.1 mA/m for the Molspin magnetometer and 2.4 μA/m for the JR-6A; calibration error was <1% for both instruments. SIRM was followed by imposition of an IRM at 0.3 T in the $-z$ direction to allow calculation of the ratio $S_{-0.3T} = [(-IRM_{-0.3T}/IRM_{1.0T}) + 1]/2$ (Bloemendal et al., 1992). Magnetic susceptibility

10.1029/2018JB017277

(SI form) was measured with Bartington Instruments MS-2 systems in both the JR and PALM laboratories, using the low-frequency (465 Hz) and ×1 sensitivity settings with correction for drift before and after each measurement. Measurements in the PALM laboratory used the MS-2B sensor, with a noise level of 2×10^{-6} and a calibration accuracy of 1%. Shipboard susceptibility measurements for discrete samples used a MS-2C loop sensor, with the output being in uncalibrated "instrument units." Subsequent intercalibration of magnetic susceptibility was achieved by measurement of reference standard samples at both the JR and PALM laboratories: this determined a correction factor for the MS-2C of 2.009. Volume magnetic susceptibility in the SI definition (κ) ranged from 140×10^{-6} to $32\,000 \times 10^{-6}$. SIRM normalized by magnetic susceptibility (SIRM/κ) has repeatedly been shown to increase in the presence of magnetic iron sulfides (Frank et al., 2007; Housen & Musgrave, 1996; Roberts, 1995; Snowball, 1991).

Major (saturated) hysteresis loops were measured to define coercivity (B_c), saturation magnetization (M_s), and saturation remanence (M_r), and DC demagnetization of M_r was measured to define coercivity of remanence (B_{cr}). Hysteresis and DC demagnetization were conducted at the Australian National University (144 samples) and Institute for Rock Magnetism (IRM; 36 samples) laboratories using similar Princeton Measurements Corporation vibrating sample magnetometers, with a maximum applied field of 1 T, averaging time of 100 ms, and 2 mT field increments. Specimens for hysteresis measurements were prepared as powders after drying and light hand-grinding in an agate mortar and pestle. The powdered samples were loaded into gelatin capsules that typically hold 0.1–0.2 g of sediment. Loops were corrected for drift and high-field slope, calculated by a linear fit of the loop above 700 mT; we note that the implicit assumption that saturation had been reached may result in some degree of overestimation of M_{rs}/M_s (Jackson & Swanson-Hysell, 2012; Roberts et al., 2018). Hysteresis results were combined to calculate the index $D_{JH} = (M_r/M_s)/(B_{cr}/B_c)$ (Housen & Musgrave, 1996), which increases as the proportion of SD ferrimagnets increases and is generally high when greigite contributes a significant proportion of the ferrimagnetic particle population.

Other analytical techniques required longer measurement times and were restricted to a smaller subset of samples selected at lower depth resolution, roughly 200–300 m apart, with additional samples in the upper 25 mbsf to examine detrital input and early diagenesis (Figure 2). These samples were intended to represent broad depth trends in magnetic mineral diagenesis rather than the response to individual fluid anomalies, so samples were taken from intervals between the anomalies. FORCs (Pike et al., 1999; Roberts et al., 2000) were determined for 12 of the hysteresis samples at the IRM laboratory using a saturating field of 1 T, with B_u ranging from −40 to +40 mT, B_c from 0 to 100 mT, an averaging time of 100 ms, a field increment of 2.34 mT, and 100 FORCs for each sample run. FORC diagrams were produced using the FORCinel 3.0 software package (Harrison & Feinberg, 2008). Low-temperature remanence and induced magnetizations were measured for six of the samples used for FORC analysis at the IRM laboratory using a Quantum Design MPMS2 system. A room temperature SIRM (RTSIRM) was applied with a field of 2.5 T, and was measured during cooling to 20 K and then during warming back to 300 K in zero field. One sample was subjected to additional warming cycles (to 300 K) of a 2.5 T low-temperature SIRM (LTSIRM) acquired at 20 K. This was carried out after prior cooling to 20 K in the presence of a saturating field ("field cooled," FC) and without ("zero-field cooled", ZFC) an applied field.

4. Results

4.1. Downhole Trends in SIRM and Hysteresis Parameters

Figure 2 shows the trends in SIRM/κ, $S_{-0.3T}$, and D_{JH} with depth. SIRM/κ is scattered around an overall decreasing trend with depth, which can be fitted as a log-linear function of depth through the relatively uniform, mud-dominated lithology of Holes U1437B and U1437D (Figures 3a and 3b). This relationship appears to persist, with little change to the fitting trend, even within the contrasting coarser-grained sequence in Hole U1437E.

$S_{-0.3T}$ is widely scattered in Hole U1437B, but the scatter decreases and the mean value increases with increasing depth through Hole U1437D, the trend culminating in the coarser-grained Units V and VI in Hole U1437E, where $S_{-0.3T}$ remains almost constant at values >0.99. Scatter toward lower values (<0.98) returns in the deepest and most coarse-grained unit, Unit VII.

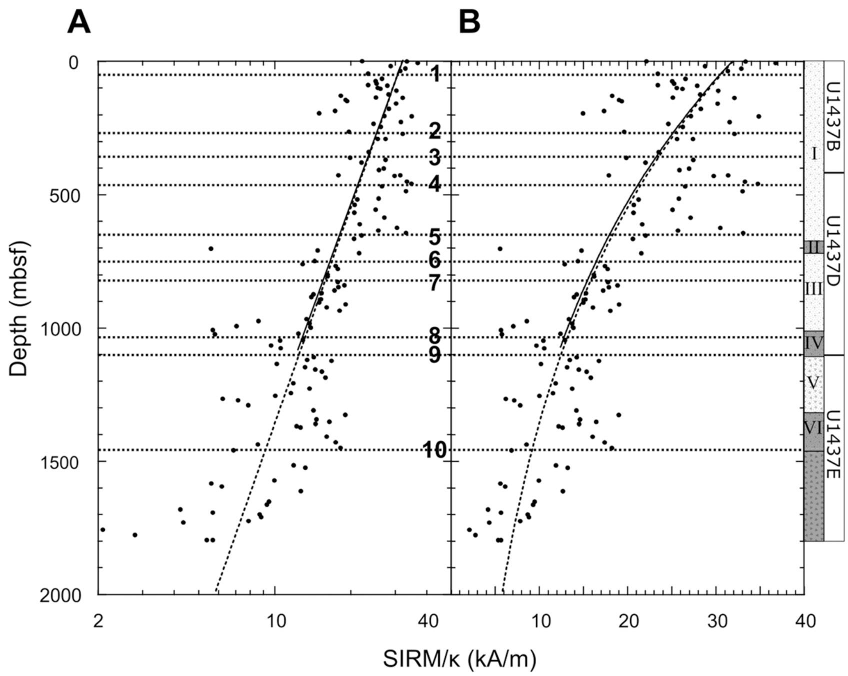

Figure 3. (a) Enlarged plot of log (SIRM/κ) versus depth for Site U1437. Numbered fluid anomalies indicated by dashed lines. The solid line is the best fit to the data in Holes U1437B and U1437D; the dashed line is the best fit to the data from all three holes. (b) The same data, on a linear plot of SIRM/κ versus depth. The solid and dashed lines are the log-linear fits shown in panel (a).

The highest D_{JH} values occur between 0 and 10 mbsf, within the initial sulfate reduction zone above fluid anomaly 1. Average D_{JH} values, and an upper envelope of D_{JH} scatter, decrease with increasing depth through Holes U1437B and U1437D; there does not appear to be a distinct trend within Hole U1437E, although the lowest cluster of D_{JH} values occurs near the bottom of the hole within Unit VII.

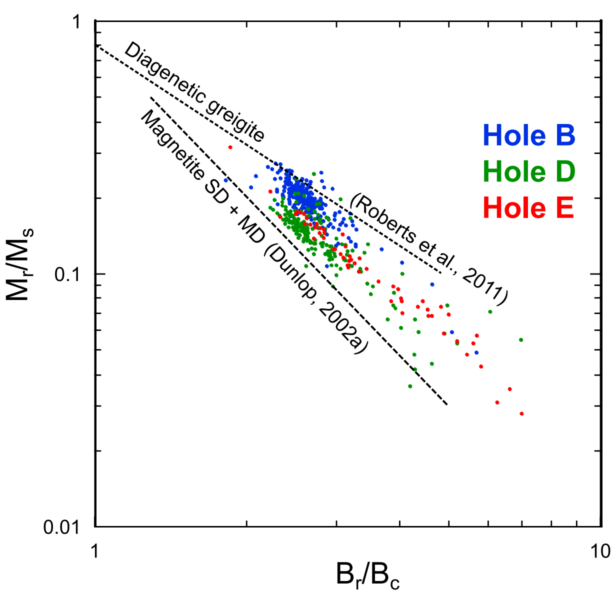

Figure 4. Day plot (Day et al., 1977) with distinct data distributions from the three holes at Site U1437. Dashed lines represent the SD–MD magnetite mixing path of Dunlop (2002a) and a compilation of data for diagenetic greigite from Roberts et al. (2011). SD = single-domain, MD = multidomain.

When plotted on a Day et al. (1977) diagram (Figure 4), hysteresis parameters define three parallel populations. Each follows a path roughly parallel to the theoretical SD–MD magnetite mixing curve of Dunlop (2002a), but the population from U1437D is displaced towards the lowest M_r/M_s ratios for a given B_{cr}/B_c ratio, and the U1437E population lies between, and overlaps, the U1437B and U1437D populations. Displacement from the theoretical curve is expected where magnetite is largely present in the vortex state (Dunlop, 2002b). However, the contrast in the amount of displacement between Holes U1437B and U1437D is surprising, if it arises purely from magnetite grain size variations, given their comparatively uniform lithologies.

Larrasoaña et al. (2007) analyzed hemipelagic sediment samples from Hydrate Ridge on the Cascadia Margin (Ocean Drilling Program, ODP, Leg 204) based on a biplot of IRM acquired at 0.9 T normalized by mass magnetic susceptibility (IRM@0.9T/χ) versus magnetic susceptibility (for which they used χ, the mass-normalized form). They defined populations dominated by fine-grained (single-domain, SD, and single-vortex state) magnetite ("Type 1", IRM@0.9T/χ < 15 kA/m and comparatively low χ), coarse-grained (multidomain, MD) magnetite ("Type 2", IRM@0.9T/χ < 15 kA/m and comparatively high χ), mixtures of magnetite and greigite ("Type 3A", IRM@0.9T/χ = 15–30 kA/m), greigite ("Type 3B", IRM@0.9T/χ = 30–60 kA/m), and pyrrhotite ± greigite ("Type 3C", IRM@0.9T/χ > 60 kA/m). Hysteresis shows our samples to

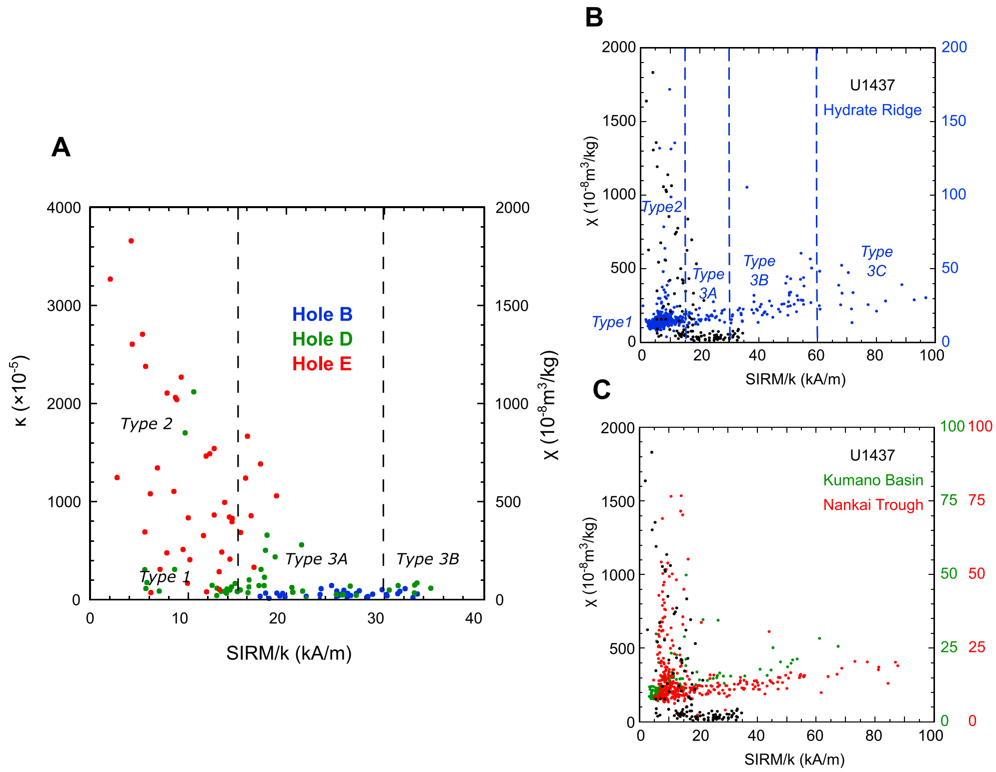

Figure 5. SIRM/ϰ versus ϰ biplot. (a) Data from the three cored holes at Site U1437. Right-hand axis converts measured volume susceptibility (ϰ) to equivalent mass susceptibility (χ), assuming an average density of 2,000 kg/m^3. Population types follow the definition of Larrasoaña et al. (2007). (b) Comparison of Site U1437 data (black dots, with χ scale on left) with data from Larrasoaña et al. (2007) (blue dots, with χ scale on right). (c) Comparison of Site U1437 data (black dots, with χ scale on left) with data from Kumano Basin (Shi et al., 2017) (green dots, with χ scale on right) and Nankai Trough (Kars & Kodama, 2015) (red dots, with χ scale on right).

be saturated, or very close to saturation, at <0.9 T, so there should be no significant quantitative difference between IRM@0.9T/χ and SIRM/ϰ (where ϰ is the dimensionless volume form of magnetic susceptibility) in our samples. Samples from the three holes at Site U1437 have distinct, if overlapping, distributions on a plot of SIRM/ϰ versus ϰ (Figure 5a). Samples from U1437B form the tightest cluster, restricted to ϰ < 200 and SIRM/ϰ ranging from about 17–34 kA/m. By contrast, Hole U1437E samples are widely distributed over a range of ϰ from <300 to >3,600, but SIRM/ϰ is restricted to <20 kA/m. Samples from Hole U1437D span the population spaces of the two other holes.

4.2. Responses Near to Fluid Anomalies

Fluid anomalies at Site U1437 are marked by local maxima or minima or breaks in trend in the SIRM and hysteresis parameters. The highest values of D_{JH}, and a local maximum in SIRM/ϰ, occur within the initial sulfate-diffusion zone above fluid anomaly 1. Proceeding downhole, fluid anomaly 1 (50 mbsf) corresponds to a sharp break to lower values in SIRM/ϰ. SIRM/ϰ recovers to above the overall trend line by about 200 mbsf, before again declining sharply below fluid anomaly 2 (270 mbsf), which also lies above sharp downhole decreases in D_{JH} and $S_{-0.3T}$. All three parameters remain low between fluid anomalies 2 and 3 (360 mbsf). SIRM/ϰ and D_{JH} increase again downhole below anomaly 3, and $S_{-0.3T}$ becomes more scattered, with both high and low values over the interval between anomalies 3 and 4 (460 mbsf). Both SIRM/ϰ and D_{JH} show a local maximum at or near anomaly 4, with the trace of both curves mimicking the sulfate profile between 400 and 500 mbsf. Elevated values of SIRM/ϰ and D_{JH} persist down to fluid anomaly 5 (650 mbsf), which marks a sharp offset to lower SIRM/ϰ and D_{JH} and higher $S_{-0.3T}$ downhole.

Fluid anomalies 6–10 are defined by enhanced methane and ethane concentrations. Anomaly 6 (750 mbsf) has a muted response in the magnetic mineralogy that is best seen in the D_{JH} profile in which there is a small but sharp decrease at anomaly 6 followed by a more gradual downhole recovery (a D_{JH} "notch"). Fluid anomaly 8 (1,035 mbsf) is marked by a similar but more prominent D_{JH} notch, which coincides with a drop in SIRM/κ below the background trend and (less precisely) a local maximum in the upper range of $S_{-0.3T}$. By contrast, fluid anomaly 7 (830 mbsf), which marks the top of the second interval of elevated methane concentration and fluid anomaly 9 (1,104 mbsf), which corresponds to the top of the third high-methane interval and the first appearance of ethane in headspace gas, both coincide with returns to above-trend SIRM/κ and the bottom of a D_{JH} notch. SIRM/κ increases downhole through most of the elevated methane and ethane interval between fluid anomalies 9 and 10 (1,460 mbsf), and $S_{-0.3T}$ is tightly grouped very close to 1 (>0.992) for all but one specimen. Below fluid anomaly 10 scatter increases in $S_{-0.3T}$, and SIRM/κ decreases downhole.

4.3. Detailed Studies (FORC and Low-Temperature SIRM Cycling)

Changes in the magnetic mineralogy with depth are revealed in more detail by the FORC and low-temperature analysis applied to the sample subset. It was not possible to process enough samples to completely characterize variation within lithostratigraphic units, but the general pattern of magnetic mineral diagenesis with depth can be seen by comparing results from the three holes. Holes U1437B (0–439 mbsf) and U1437D (427–1,104 mbsf) are dominated by the lithologically similar Units I and III, and any changes should mostly reflect diagenesis rather than differences in detrital input. Hole U1437E (1,104–1,806 mbsf) contrasts with the shallower holes, with a shift to coarser, more proximally derived volcaniclastics in Units VI and VII: changes in rock magnetic parameters in this deepest hole may reflect both deep diagenesis and variation in source.

4.3.1. Hole U1437B (Unit I)

Samples from core U1437B-1H (Figures 6a, 6b, and supporting information Figure S2), taken just below the top of the sediment column at the top of Hole U1437B, illustrate the detrital input in the mud-dominated units. FORCs lack a well-defined central ridge along $B_u = 0$. Absence of a clear central ridge suggests that contributions from intact magnetosomes from magnetotactic bacteria (Egli et al., 2010; Heslop et al., 2014) are limited. FORC diagrams from the top of Hole U1437B have low-coercivity FORC distributions, with most of the signal below 10 mT and an asymmetric distribution that does not diverge strongly from the $B_u = 0$ axis until $B_c < 10$ mT. Comparison with the examples of FORC distributions in Roberts et al. (2000, 2014, 2017) suggests a mixture of vortex-state, MD and SP responses.

At a depth of 40.5 m (Figure 6c) the FORC distribution shows higher coercivity, with the distribution peaking between 15 and 40 mT, and at least two populations are present. This FORC pattern continues through Hole U1437B (Figure 6e).

Low-temperature cycling of RTSIRM was measured in two samples from Hole U1437B, at 40.5 mbsf (Figure 6d) and 146.3 mbsf (Figure 6f). The sample at 40.5 mbsf has a peak in $-\Delta M/\Delta T$ on the cooling curve at about 110–115 K (inset in Figure 6d), representing the Verwey transition of magnetite (Muxworthy & McClelland, 2000; Verwey, 1939). This also appears in the sample at 146.3 mbsf, although the peak is less sharp and shifted to 90–100 K (inset in Figure 6f). RTSIRM in both samples is not reversible over the cooling-warming cycle, having the large remanence loss below the Verwey temperature (T_V) that is characteristic of MD magnetite grains (Halgedahl & Jarrard, 1995). M'_{300}/M_{300} (where M_{300}, is the original RTSIRM, and M'_{300} is the RTSIRM remaining after cycling) has values of 0.81 (40.5 mbsf) and 0.88 (146.3 mbsf) (Table 1). RTSIRM warming curves also display a distinct "hump" resulting from the combination of a uniformly negative $\Delta M/\Delta T$ path above T_V and the recovery of magnetic memory across the Verwey transition (Halgedahl & Jarrard, 1995), which together produce a local magnetization peak at about 150 K, and $M'_{300} < M_{20}$ (the RTSIRM after cooling to 20 K). A single peak in $\Delta M/\Delta T$ on the cooling path at about 110–115 K suggests nearly stoichiometric magnetite, with a low degree of oxidation (Özdemir et al., 1993). The U1437B samples show no clear evidence for the presence of the Morin transition of hematite (Morin, 1950; Özdemir et al., 2008), which occurs at a temperature (T_M) of about 250–260 K for grains >0.1 μm but at lower temperatures for smaller grains. Freezing of residual brines in pore water may have disturbed the sediment to produce a "transition imposter," an apparent loss of magnetization due to physical disturbance of grain alignment (Bowles et al., 2010), at about 265 K in the sample at 40.5 mbsf (Figure 6f).

10.1029/2018JB017277

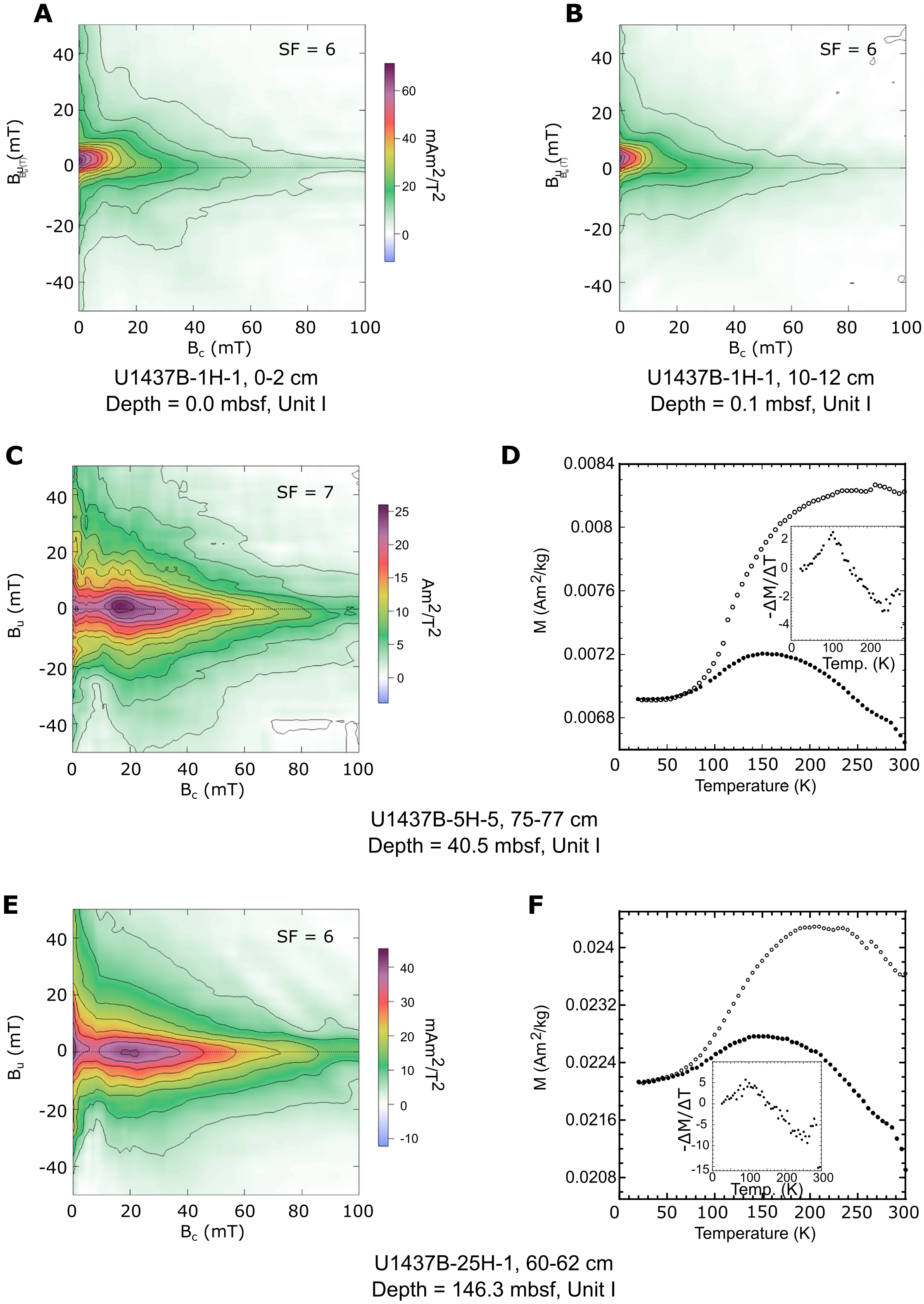

Figure 6. First-order reversal curve (FORC) diagrams (a, b, c, and e) and plots of low-temperature room temperature saturation isothermal remanent magnetization (RTSIRM) cycles (d, f) for samples from Hole U1437B. SF = FORC smoothing factor. RTSIRM cooling curves are indicated by open symbols; warming curves by closed symbols. M = magnetization. Insets in RTSIRM cycle plots show the negative of the rate of change of magnetization with temperature during the cooling cycle ($-\Delta M/\Delta T$), with units of 10^{-5} A/m^2/kg.

10.1029/2018JB017277

Table 1
RTSIRM Cycling Parameters, Site U1437

Sample ID	Depth (mbsf)	Unit	M'_{300}/M_{300}	ΔM_{inv}
U1437 ...				
B-5H-5, 75–77cm	40.5	I	0.81	1.94
B-25X-1, 60–62 cm	146.3	I	0.88	2.90
D-2R-1, 35–37 cm	427.6	I	0.78	3.05
D-42R-1, 53–55 cm	816.0	III	0.77	1.48
D-72R-3, 39–41 cm	1,087.9	IV	0.57	0.86
E-24R-2, 38–40 cm	1,283.0	V	0.64	0.41

4.3.2. Hole U1437D (Units I–IV)

The FORC distribution from a sample from the first core of Hole U1437D, at 427.6 mbsf (Unit I), contains signs of a decreased proportion of the higher-coercivity population(s) (Figure 7a). Deeper in this hole, at 816.0 mbsf (Unit III) (Figure 7c), almost all the higher-coercivity population has disappeared, and the outer contours of the distribution have a divergent pattern typical of a dominantly multivortex to MD population (Lascu et al., 2018; Roberts et al., 2000, 2017). The lower-coercivity and coarsening magnetic grain size is even more extreme in the deepest sample from Hole U1437D, at 1,087.9 mbsf (Unit IV) (Figure 7e).

RTSIRM in samples from Hole U4137D continues to show a nonreversible loss of remanence T_V, and the proportion of the recovered remanence measured by M'_{300}/M_{300} decreases from 0.78 at 427.6 mbsf (Figure 7b) to 0.57 at 1,087.9 mbsf (Figure 7f), consistent with the FORC evidence for an increasing dominance of MD grains. The sample at 816.0 mbsf (Figure 7d) has a broader Verwey transition peak (T_V) in the $-\Delta M/\Delta T$ plot between about 114 and 120 K. This peak broadening is more dramatic for a sample from the comparatively coarse-grained Unit IV (1,087.9 mbsf, near the base of Hole U1437D) (Figure 7f), in which there are two distinct $-\Delta M/\Delta T$ peaks at about 95 and 119 K. The lower-temperature peak may represent a distinct population of grains, characterized by either a higher degree of surface maghemitization or a higher degree of Ti substitution, both of which processes result in decreased T_V (Moskowitz et al., 1998; Özdemir & Dunlop, 2010). The enhancement of this second population presumably represents an increased contribution of volcaniclastic grains in Unit IV, compared to Units I and III. Double T_V peaks have also been attributed to mixed biogenic and detrital magnetite assemblages (Chang, Heslop, et al., 2016), but the continued lack of a biogenic signal in the corresponding FORC diagram argues against the presence of significant proportions of biogenic magnetite in Unit IV. Samples at 428 mbsf (Unit I) (Figure 7b) and 1,088 mbsf (Unit IV) (Figure 7f) show inflections during RTSIRM cooling at 234 and 244 K, respectively. These temperatures are too low to be likely results of brine freezing so may represent the hematite Morin transition in very fine grains.

The sample at 427.6 mbsf, which lies within the sulfate diffusion profile between fluid anomalies 3 and 4 in Unit I, was additionally subjected to FC and ZFC measurements during warming from low temperature (Figure 8). The ratio of remanence lost at T_V for field-cooled versus zero-field-cooled cycles, δ_{FC}/δ_{ZFC} = 0.98 (Moskowitz et al., 1993), indicating that intact magnetosomes do not contribute significantly. The parameter D of Passier and Dekkers (2002), which compares the average values of the FC and ZFC warming curves above T_V, has a small, negative value of −0.01, which suggests that, for this sample at least, there are few defects resulting from surface oxidation (maghemitization) of magnetite. The FC and ZFC paths for this sample track closely together, except below about 50 K, where the FC curve is higher, and both FC and ZFC warming curves decrease rapidly between 20 and 50 K and continue to decrease above T_V. When MD magnetite is the dominant remanence carrier, the ZFC curve is usually higher than the FC curve, at least up to T_V (Carter-Stiglitz et al., 2006), and most of the remanence is lost in a steep decrease around the Verwey transition. Brachfeld et al. (2002) attributed similar FC/ZFC curve behavior to that shown in Figure 8 to the presence of mixed "PSD" (vortex state) and SP grains. The combination of the highly irreversible RTSIRM paths and the FC/ZFC behavior implies the presence of both MD magnetite and an additional significant contribution from finer grains of either magnetite or greigite, including SD grains that become thermally activated to exhibit SP behavior during low-temperature warming (Banerjee et al., 1993; Passier & Dekkers, 2002).

4.3.3. Hole U1437E (Units IV–VII)

MD behavior continues to dominate FORC distributions in samples from 1,283.0 mbsf (Unit V) and 1585.1 mbsf (Unit VII) (Figure 9A, C) in Hole U1437E, but a sample from 1797.1 mbsf (Unit VII) (Figure 9d), the deepest rock magnetic sample studied at the site, contains an additional higher-coercivity component with SD-like contours in the lower left of the plot.

RTSIRM cycling in the sample at 1,283.0 mbsf (Figure 9b) confirms a dominantly MD distribution, with M'_{300}/M_{300} =0.64. Twin T_V peaks are again present in $-\Delta M/\Delta T$ in this sample. The magnitude of the RTSRIM warming hump continues the reduction with increasing burial depth seen through Hole U1437D.

10.1029/2018JB017277

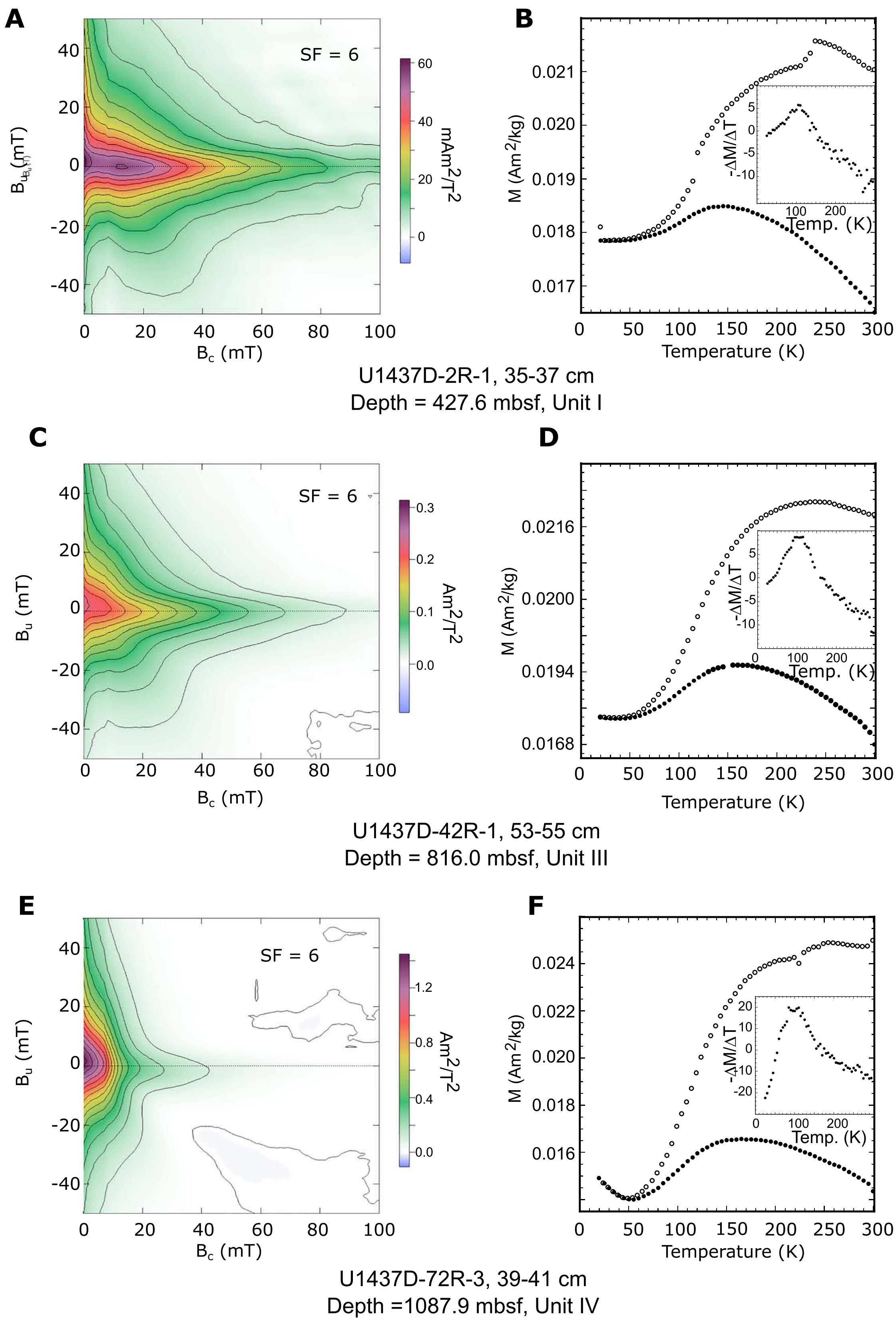

Figure 7. FORC diagrams (a, c, and e) and plots of low-temperature RTSIRM cycles (b, d, and f) for samples from Hole U1437D. Symbols and abbreviations as in Figure 6.

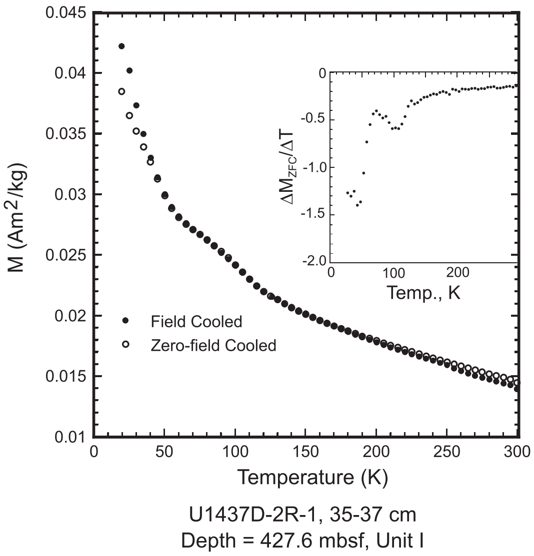

Figure 8. Warming trends of field-cooled (solid symbol) and zero field-cooled (open symbol) LTSIRM for sample from 427.6 mbsf. Inset is for warming $\Delta M/\Delta T$ of a zero field-cooled LTSIRM, with units of 10^{-3} A/m^2/kg. LTSIRM = low-temperature saturation isothermal remanent magnetization.

5. Discussion

5.1. Detrital Input

Detrital magnetic mineral input to the tuffaceous mud that dominates the upper 1,300 mbsf of the studied sequence (Units I, II, and V) is dominated by magnetite, which reflects its volcanic arc source. Magnetotactic bacteria are at most a minor contributor to the magnetic mineral assemblage, although high-resolution FORC analyses in a detailed study of samples from the upper 100 m of Hole U1437B (Kars et al., 2017) do display a weak central ridge, suggesting a small biogenic component. RTSIRM results also indicate that surface oxidation of magnetite is limited in the muds, although it may increase (or Ti content may increase) in the volcaniclastic-dominated units in the deeper part of the sequence. MD magnetite grains are revealed by nonreversible RTSIRM paths in all samples from U1437, and FORC diagrams from the first core indicate that the detrital input comprises a magnetically soft mix of MD, vortex state, and SP grains.

$S_{-0.3T}$ is restricted to values >0.945 through the whole studied sequence (Figure 2), which indicates that ferrimagnets dominate the magnetization of all samples. Samples with scattered low values <0.96 occur in the upper 200 mbsf of Unit I, which corresponds to the interval studied in detail by Kars et al. (2017), who inferred the presence of detrital hematite in the continental hemipelagic mud component from the presence of a high-coercivity fraction. However, neither that study, nor the present work, identified Morin transitions within the upper part of Unit I, which suggests that any hematite present is fine-grained (Özdemir et al., 2008) or contributes substantially less to the net magnetization than the ferrimagnetic components. Other sets of samples with relatively low $S_{-0.3T}$ occur in the deeper part of Unit I, and in coarse-grained Units V and VII, which lack hemipelagic inputs. The presence of hematite in these intervals is supported by the tentative observation of Morin transitions in samples from 427.6 mbsf in Unit I (Figure 7d) and from 1,087.9 mbsf in Unit IV (Figure 7f). None of the $S_{-0.3T}$ values are low enough to provide conclusive evidence for hematite; however, and $S_{-0.3T}$ decrease may alternatively be attributed to higher-coercivity ferrimagnets, which could include greigite or pyrrhotite (Roberts et al., 2010), or elongated or maghemitized magnetite. Bacterial magnetite magnetosomes, which could contribute a higher-coercivity component (Kruiver & Passier, 2001), can be largely ruled out as a source of low $S_{-0.3T}$ by the FORC evidence.

5.2. Progressive Magnetic Mineral Diagenesis

The detrital magnetic mineral input, dominated by magnetite, undergoes progressive modification throughout the sequence at Site U1437. Reduction of sulfate, supplied both from diffusion from the seafloor and by later fluid inputs, can be expected to have driven the successive stages of partial magnetite dissolution, greigite formation, and eventual pyritization of greigite constituting sulfidic diagenesis (Roberts, 2015). Rock magnetic evidence for greigite can be ambiguous (Roberts et al., 2011), but greigite may be responsible for the humps in the RTSIRM warming curves (Figure 10). Such humps arise from the superposition of the magnetite Verwey transition and a monotonically decreasing trend during warming in a phase which does not exhibit a transition. This behavior has commonly been interpreted to mark partial maghemitization of magnetite by surface oxidation (Chang et al., 2013; Channell & Xuan, 2009; Özdemir & Dunlop, 2010). However, within Unit I at least, the low-temperature behavior suggests limited oxidation. Diagenetic greigite, largely in the SD to SP size range, produces similar monotonic trends during RTSIRM cycling to those of maghemite (Chang et al., 2009, 2013), and a population of MD or single-vortex magnetite and diagenetic greigite (± maghemite) would yield the observed RTSIRM curves.

We use the ΔM parameter of Chang et al. (2013), which is designed to emphasize the scale of the hump in reversible RTSIRM cooling-warming cycles produced by partially oxidized magnetosomes and invert it to produce a new parameter, ΔM_{inv}, to measure the greigite contribution (possibly together with that of maghemite below Unit I) relative to magnetite in nonreversible RTSIRM warming curves for Site U1437

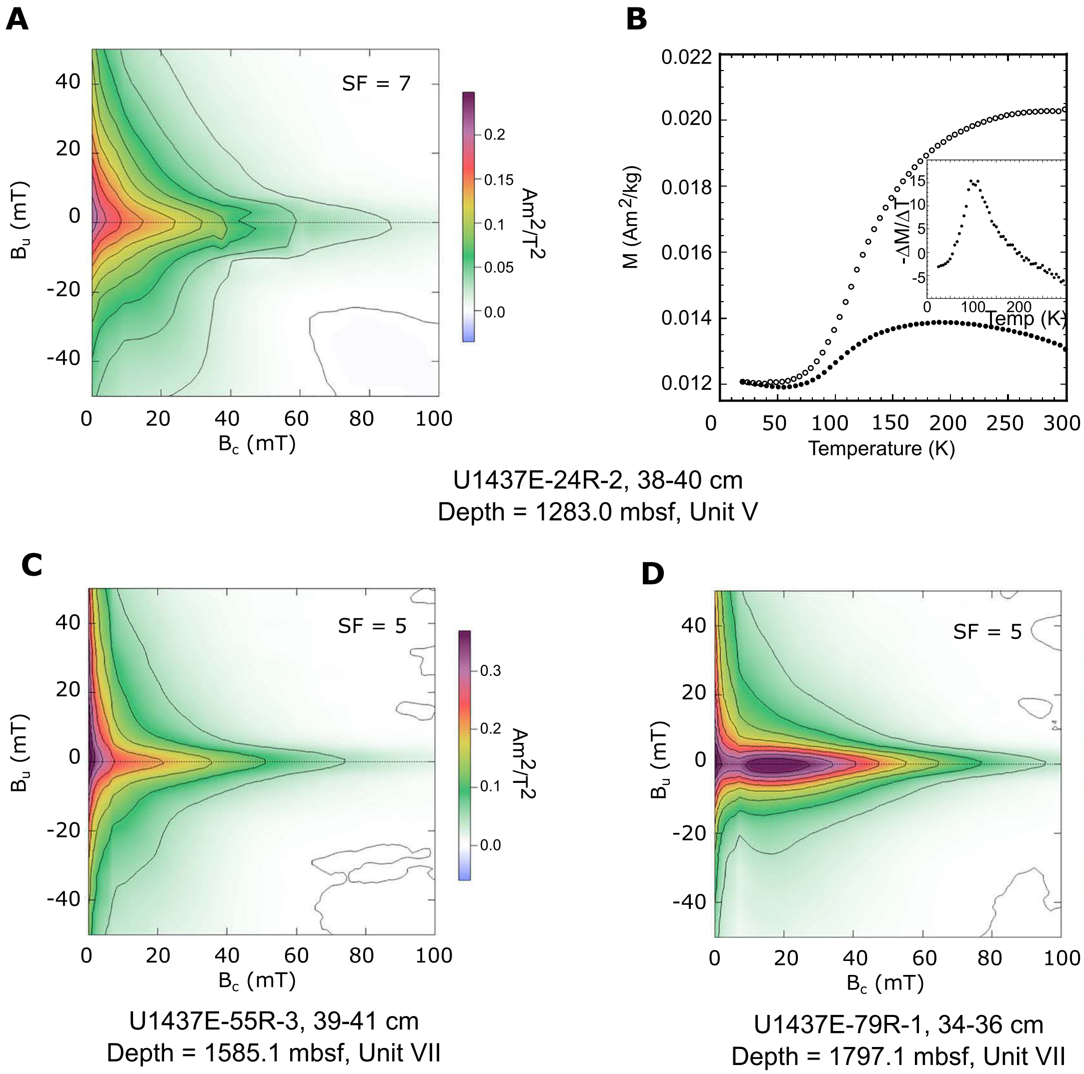

Figure 9. FORC diagrams (a, c, and d) and plot of low-temperature RTSIRM cycles (b) for samples from Hole U1437E. Symbols and abbreviations as in Figure 6.

(Table 1). We define $\Delta M_{\text{inv}}= (M_{\text{max}} - M'_{300})/(M_{\text{max}} - M_{\text{min}})$, where M_{max} is the maximum value on the warming curve at temperatures above the Verwey transition and M_{min} is the minimum value below T_V. Within our limited sample set, ΔM_{inv} appears to increase progressively with depth within Unit I from 1.94 at 40.5 mbsf to 3.05 at 427.6 mbsf, before declining steadily with depth through the more volcaniclastic-rich Units II, IV, and V.

Our interpretation of the ΔM_{inv} data is supported by the SIRM/ϰ versus ϰ plot (Figure 5a). Samples from Site U1437 define three separate populations similar to those recognized in magnetic-sulfide-bearing hemipelagic sediments at Hydrate Ridge by Larrasoaña et al. (2007), although the volcanic-rich detrital input at Site U1437 extends the magnetic susceptibility range of each population to much higher values than those defined by the hemipelagic suite at Hydrate Ridge (Figure 5b). SIRM/ϰ is independent of the concentration of magnetic grains, depending principally on mineralogy and grain size, so addition of magnetite, much of it in the MD range, should, if anything, reduce the range of the plots on the SIRM/ϰ axis. Similar distributions, again restricted to much smaller magnetic susceptibility ranges, have also been reported from mixed magnetite-greigite assemblages from Kumano Basin (Shi et al., 2017) and Nankai Trough (Kars & Kodama, 2015) (Figure 5c), both representing hemipelagic slope sediments with minor admixes of volcanic ash. Allowing for the greater magnetic susceptibility range, samples from Hole U1437B (Unit I) are classified as Type 3A (magnetite + greigite) and 3B (greigite dominated), samples from Hole U1437D (Units I–IV) are

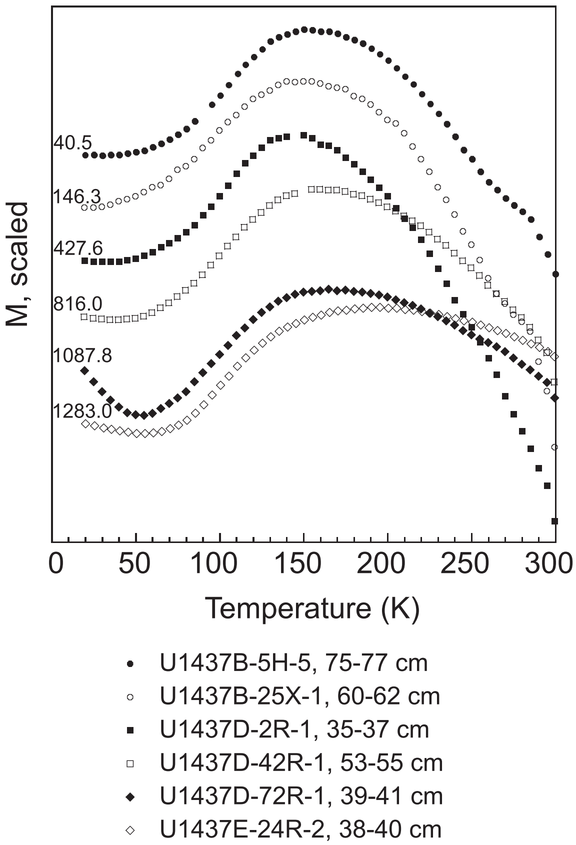

Figure 10. Comparison of RTSIRM warming curves from Site U1437, which illustrate the varying size of the "hump" resulting from inferred superposition of the MD magnetite Verwey transition and the negative $\Delta M/\Delta T$ contribution of greigite and maghemite. Data are normalized so that the memory recovery across the Verwey transition scales the same ($M/(M_{\max} - M_{\min})$). The position on the M axis is arbitrary, and the plots are stacked in order of sample depth.

classified as a mix of Types 1 (SD/vortex-state magnetite dominated), 2 (MD magnetite dominated), and the greigite-bearing Types 3A and 3B, and Hole U1437E (Units IV–VII) samples are restricted to Types 1 and 2.

Differences between the Day plot mixing trends for Holes U1437B and U1437D (Figure 4) resemble those seen for samples from ODP Site 889/890 on the Cascadia Margin (Shipboard Scientific Party, 1994: Housen & Musgrave, 1996), where the trend further from the magnetite SD + MD mixing curve represents samples from an interval with higher proportions of magnetic iron sulfides, probably greigite. Roberts et al. (2011) compiled a global data set for diagenetic greigite and showed that these data plot along a power law trend on the Day plot, which represents a SD + SP mixing trend. Samples from Hole U1437B are displaced toward this plot, which supports other evidence that diagenetic greigite is present in larger proportions in Hole U1437B than in Hole U1437D. Why samples from Hole U1437E define an intermediate distribution is unclear, but it could reflect differences in the detrital input between the volcaniclastic-dominated units that dominate this hole and the muds and mudstones that comprise most of the sequence in the shallower holes.

Sulfidic alteration in response to AOM has been reported to generate monoclinic pyrrhotite (Kars & Kodama, 2015; Larrasoaña et al., 2007). No unambiguous rock-magnetic evidence for pyrrhotite is provided in any samples from this study, but Kars et al. (2018) in their study of Site U1437 recognized a candidate for the Besnus transition of pyrrhotite (Dekkers et al., 1989; Rochette et al., 1990) at ~32 K in ZFC LTSIRM warming curves for samples in intervals with lower methane contents within the overall methane-rich zone between fluid anomalies 6 and 8. Diagenetic pyrrhotite which forms in methanic sediments has been reported to lack a Besnus signature (Horng & Roberts, 2018), so the presence of diagenetic pyrrhotite in the methane-rich zones cannot be ruled out.

FORC distributions allow some separation of individual components that contribute to progressive diagenetic changes. Appearance of a bimodal distribution in the upper part of Unit I, which is marked by a sample at 40.5 mbsf (Figure 6c), reflects addition of a new, higher-coercivity phase to the detrital vortex—MD magnetite assemblage, with at least part of the new component in the SD range. This new phase, which is likely to be diagenetic greigite, persists through Hole U1437B, but declines in significance with increasing depth in Holes U1437D and U1437E. The bimodal coercivity distribution of the sample from Unit VII at 1,797.1 mbsf (Figure 9d) is exceptional, but may be unrelated to this progressive diagenetic change; the coarser fraction sampled in Unit VII may include silicate grains with SD magnetite inclusions (Chang, Roberts, et al., 2016), which have been shielded from the dissolution which has removed SD magnetite from all finer-grained samples.

Combining the rock magnetic evidence yields an overall downhole progression of magnetic mineral diagenesis at Site U1437. Greigite constitutes a relatively high proportion of the total magnetic mineralogy through Unit I and decreases in concentration in the lower units. Elevated proportions of greigite persist below the initial SMT, which at U1437 occurs between 20 mbsf (local methane maximum) and 50 mbsf (fluid anomaly 1, defined by the base of the shallow sulfate diffusion profile), and continue through most of Unit I, before decreasing sharply at fluid anomaly 5. Magnetic susceptibility (supporting information Figure S3) remains largely unchanged across the SMT and throughout Unit I, which indicates that greigite authigenesis and dissolution of the fine-grained magnetite fraction roughly compensate for each other. This contrasts with the situation in some sulfidic hemipelagic settings, where greigite growth is a minor by-product of near-complete reductive dissolution of magnetite at the SMT, with most of the iron sulfide being fully reduced to pyrite, resulting in a precipitous decrease in the magnetic susceptibility, for example, the Oman margin and Northern Californian margin (Rowan et al., 2009) and the Ontong Java

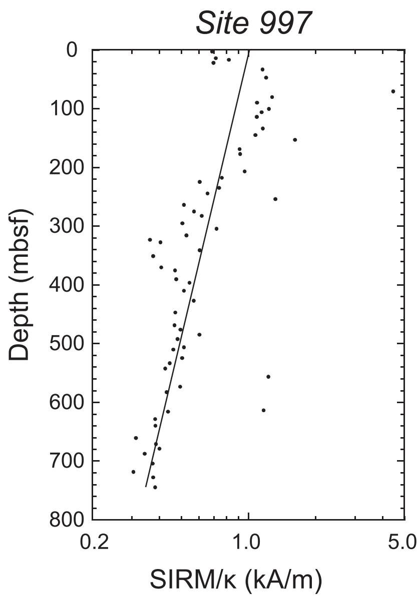

Figure 11. Log (SIRM/κ) versus depth from Ocean Drilling Program Site 997 on Blake Ridge. The solid line shows log-linear interpolation of background decrease in SIRM/κ with depth (Shipboard Scientific Party, 1996b). SIRM = saturation isothermal remanent magnetization.

Plateau (Musgrave et al., 1993). Magnetic susceptibility of the detrital input is much higher at Site U1437 (averaging about 500×10^{-6} SI in the upper 50 m of Unit I) than at the Oman and Northern California margins (both about 10–40 $\times 10^{-6}$ SI) or Ontong Java Plateau (about 100×10^{-6} SI), and total organic carbon is lower (<1% at U1437, versus 1–2% for the Oman margin and 2.8% for the Northern California margin). The comparatively limited decrease in magnetic susceptibility across the SMT at Site U1437 suggests that reduction there is limited by the lower ratio of organic matter to magnetite in the detrital input; similar organic content control on the extent of magnetite reduction has also been noted in other settings (e.g., Channell & Hawthorne, 1990). Magnetite at Site U1437 may have also been protected from dissolution by comparatively coarse grain sizes (MD grains make up a significant component of the detrital input) and by occurring as inclusions within silicates, as observed in IODP Site C0002 on the Nankai margin (Shi et al., 2017). No true methanic zone is present below fluid anomaly 1, with concentrations limited to <6 ppmv until fluid anomaly 6, presumably because methane is largely consumed by AOM driven by sulfate diffusing from inputs at fluid anomalies 2 and 4. The resulting H_2S may result in additional magnetite dissolution and greigite authigenesis, but the take-up of sulfide by Fe^{2+} still exceeds the supply, limiting further conversion of greigite to pyrite and so maintaining high SIRM/κ values.

Samples from Units I through to near the bottom of Unit III (Figures 6a–6c, 7a, and 7c) show evidence for vortex-state magnetite in their FORC diagrams. FORC diagrams of samples from the deepest part of Hole U1437D and on through Units V–VII in Hole U1437E are dominated by MD grains (Figures 7e, 9a, and 9c), except where SD magnetite survives as silicate inclusions (Figure 9d). This may partly reflect the coarser detrital input in the older part of the sequence, but it also represents a culmination of the magnetite reduction trend.

The SIRM/κ trend with depth, which is generally high in Unit I and decreases downhole, appears to continue even into Hole U1437E, despite the change in lithology to the volcaniclastic-dominated Units VI and VII. Changes in SIRM/κ can be understood in terms of the distribution of samples on the SIRM/κ versus κ biplot of Figure 5a. Greigite and magnetite are both present in most, if not all, samples below the near-seafloor SMT, with variations in the proportions of the two being responsible for the change from a Type 3A and 3B distribution in Hole U15437B to a mix of Types 1, 2, 3A, and 3B in U1437D, and to a mixed Type 1 and 2 distribution in U1437E. Reduction in the proportion of greigite through pyritization shifts the balance of the distribution toward the low SIRM/κ fields of Type 1, regardless of any resulting change in κ, and so results in a decrease in SIRM/κ.

A similar log-linear SIRM/κ decrease with depth has been reported for more lithologically uniform hemipelagic drift sediments from Blake Ridge cored on ODP Leg 164 (Figure 11) and was attributed to slow conversion of greigite to pyrite through prolonged exposure to low sulfide concentrations (Shipboard Scientific Party, 1996a, 1996b). IODP Site C0002, which sampled gas hydrate-bearing forearc basin and prism sediments from the Nankai margin, likewise has a progressive downhole SIRM/κ decrease from peak values developed in the greigite-rich gas hydrate zone (Shi et al., 2017). At least some of the downhole decrease in SIRM/κ at Site U1437 probably reflects a shift to lower coercivities (dominantly MD sizes) in the magnetite population, as finer magnetite grains are selectively dissolved and the lithology changes from mud- to volcaniclastic-dominated, but increasing pyritization of greigite probably also plays a significant role.

Sedimentation rates across Units I through V varied between 98 and 259 m/My, but mostly did not deviate far from a mean of about 165 m/My (Tamura et al., 2015), so log (SIRM/κ) is also approximately linear with respect to depositional age. Such a relationship suggests a slow pyritization process continuing at a background rate long after early magnetic diagenesis is completed. Continued pyritization of greigite requires a deep sulfide supply (Rowan et al., 2009), which at Site U1437 is partly supplied by reduction of deep sulfate inflows and direct H_2S input associated with migrating methane and ethane. Deeply sourced sulfide, even in the absence of fluid inputs, appears to be responsible for progressive pyritization in hemipelagic sequences far below the SMT (Shipboard Scientific Party, 1996b). This deep sulfide may be a product of AOM-driven reduction of sulfate liberated by anaerobic oxidation of pyrite (Bottrell et al., 2000; Larrasoaña et al., 2007). Similar slow supply of sulfide may also be responsible for the background trend toward pyritization at Site U1437, which is evident in the log-linear trend line in the SIRM/κ profile, and which continues outside the intervals influenced by the fluid incursion anomalies. Magnetite dissolution and greigite pyritization are progressive processes at Site U1437 and extend well below the near-surface sulfidic zone and continue at a slow rate throughout the 15 My history of deposition at the site.

Unlike many hemipelagic sequences in which a large decrease in magnetite concentration occurs below the SMT, magnetite dissolution at U1437 is limited, with at least some vortex state magnetite surviving to at least 1,000 mbsf, and MD magnetite and some probable SD magnetite inclusions occur to the bottom of the hole at 1,800 mbsf. Nankai margin sediments from IODP Site C0002 (Shi et al., 2017) similarly preserve MD magnetite and finer magnetite inclusions despite enhanced diagenetic dissolution in zones of high methane concentration as either gas hydrate of free gas. Both a high proportion of magnetite relative to organic content in the detrital input, and a degree of protection from dissolution afforded to magnetite by large grain size or by occurring as inclusions within silicates, are important factors in survival of significant quantities of detrital magnetite through progressive diagenesis.

Despite the relatively high geothermal gradient inferred at Site U1437, which predicts that the 50 °C threshold for the magnetite window observed in the burial diagenesis of claystones by Aubourg et al. (2012) would be reached at about 570 mbsf, there appears to be no evidence of significant growth of new magnetite. Likewise, temperatures exceeding 65 °C (the predicted temperature at 750 mbsf, the depth of fluid anomaly 6) do not seem to be an impediment to new generations of greigite growth at fluid anomalies 7 and 9 in the methane and ethane zones, although other studies suggest that greigite is only significant at burial temperatures <60 °C (Kars et al., 2014). Variations in detrital magnetite and organic input, and added complexity from deep incursions of sulfate and hydrocarbon-bearing fluids, clearly complicate simple models of burial diagenesis of magnetic minerals.

Infiltration of sulfate-rich fluids deep below the seafloor has been reported from convergent continental margin settings (Expedition 334 Scientists, 2012; Shipboard Scientific Party, 1997), but its impact on magnetic mineral diagenesis has not been examined. Site U1437 demonstrates the potential for sulfate inflow to locally stimulate greigite authigenesis, even in a sequence that has already experienced an initial phase of sulfide reduction in the near-seafloor sulfidic zone. Methane migration and accumulation is also a common feature of convergent margin settings, but most existing studies of the influence of methane on late diagenesis have focused either on modern gas hydrate settings (Horng & Chen, 2006; Housen & Musgrave, 1996; Kars & Kodama, 2015; Larrasoaña et al., 2007; Musgrave et al., 2006) or have inferred the likelihood of past gas hydrate accumulations (Roberts et al., 2010; Rowan & Roberts, 2008; van Dongen et al., 2007). Gas accumulations at Site U1437 lie far below the base of potential gas hydrate stability and appear to be controlled by migration along faults and accumulation in porous reservoirs; our results extend the record of AOM to deep methane at relatively high temperatures. Sulfide accumulating with methane as sour gas also appears to be a factor in enhancing conversion of greigite to pyrite.

5.3. Punctuated Magnetic Mineral Diagenesis

Superimposed on the progressive trends of increasing magnetite dissolution and conversion of greigite to pyrite at Site U1437 are a series of features seen on the SIRM/κ profile, where values cluster above or below the background trend. We interpret the correspondence of many of these clusters with the fluid anomalies recognized in the pore water and headspace gas analyses as evidence that they represent local intervals of renewed or enhanced magnetic mineral diagenesis, which locally oppose or enhance the background trend. We term this behavior "punctuated diagenesis." In some cases (fluid anomalies 1, 3, 6, and 8) this results in decreased coercivity, presumably by selective destruction of SD or vortex state grains of either magnetite (by dissolution) or greigite (by conversion to pyrite), while in others (fluid anomalies 2, 4, 5, and 9) it enhances coercivity, which in most of the sequence appears to be due to repeated phases of greigite authigenesis, based on the SIRM/κ response and the lack of evidence for significant proportions of SD magnetite or pyrrhotite. Possible mechanisms for greigite authigenesis may involve neoformation on pyrite grains (Jiang et al., 2001) as seen in SEM images from Hole U1437B (Musgrave & Kars, 2016), on authigenic smectite and chlorite (Roberts & Weaver, 2005) and possibly on siderite (Sagnotti et al., 2005). The relationships of these diagenetic processes to the fluid anomalies at Site U1437 are complex.

Diffusion of sulfate from the seafloor drives initial sulfate reduction, which is complete at fluid anomaly 1. The highest D_{JH} values, and a local SIRM/κ maximum, occur within this sulfate diffusion zone, and reflect greigite authigenesis. Fluid anomaly 1 is marked by a sharp break to lower values in the SIRM/κ profile, which suggests that pyritization of the first generation of greigite has occurred by renewed sulfide production in the "inverted" sulfate diffusion profile above fluid anomaly 2. SIRM/κ recovers to above the overall trend line by about 130 mbsf, which marks a second generation of greigite formation between anomalies 1 and 2. Increased Fe^{2+} concentrations below fluid anomaly 1 (supporting information Figure S1) presumably reflect excess Fe^{2+} relative to sulfide that restricts further pyritization of this greigite. This pattern appears to be repeated by the even more sulfate-rich source at anomaly 4, with a decrease in SIRM/κ and D_{JH} between anomalies 2 and 3 followed downhole by a renewed increase to a local maximum in both at or near anomaly 4, which suggests a third greigite generation in response to the renewed influx of sulfate at anomaly 4.

Elevated SIRM/κ and D_{JH} values persist down to anomaly 5. Anomaly 5 has a subtle expression in the sulfate profile, but it again marks a local culmination in greigite authigenesis, below which sharp offsets to lower SIRM/κ and D_{JH} and higher $S_{-0.3T}$ suggest a shift to a different magnetic mineral assemblage in which greigite makes a smaller contribution, presumably as a result of more complete pyritization. Increased pyritization suggests that H_2S may be concentrated below anomaly 5.

The notches in the D_{JH} profiles at fluid anomalies 6 and 8 (and possibly also below anomaly 5) resemble features seen below the base of the gas hydrate zone in sites from the Cascadia Margin, which were attributed to a reduction in the concentration of greigite resulting from its conversion to pyrite (Musgrave et al., 2006). This enhanced pyritization in the gas hydrate setting has been suggested to be the result of an accumulation of H_2S in company with methane ("sour gas") below an impermeable seal formed by gas hydrate filling porosity (Housen & Musgrave, 1996). We consider likewise that H_2S-rich horizons are responsible for the D_{JH} notches at Site U1437, with the seals in this case provided by intervals of less porous clay (Kars et al., 2018).

Fluid anomaly 7, which marks the top of the second interval of elevated methane concentration, and fluid anomaly 9, which corresponds to the top of both the third high-methane interval and the first appearance of ethane in headspace gas, both coincide with returns to above-trend SIRM/κ and the bottom of a D_{JH} notch. Higher concentrations of hydrocarbons in the intervals below anomalies 7 and 9 appear to be responsible for SIRM/κ values above the trend line, and may be acting to renew greigite growth. Kars et al. (2018) suggested the formation of relatively fine, SP greigite in the approximately 100-m interval below anomaly 7, but at least some of this must be in the SD range to explain the elevated SIRM/κ values.

SIRM/κ remains elevated above background values throughout the elevated methane and ethane interval between fluid anomalies 9 and 10, but $S_{-0.3T}$ has tightly grouped values close to 1 (>0.992) for all but one specimen. A mixture of SD and SP greigite, and the near-total dissolution of fine-grained magnetite, may explain the contrasting coercivity indicators. Lower SIRM/κ below anomaly 10, and the increased spread of $S_{-0.3T}$ to lower values, reflects a return to lower proportions of greigite as hydrocarbon concentrations drop.

5.4. Impact on Paleomagnetic Record

Magnetic polarity stratigraphy can be traced at Site U1437 from the seafloor to the base of Unit V at 1,320 mbsf, although the extent to which the depositional remanence was obscured by drilling-induced remanences and other overprints increased deeper in the sequence as MD grains increasingly dominated the signal (Musgrave & Kars, 2016). Ghost polarity intervals found at intervals within the sequence resulted from episodes of early diagenetic greigite growth within the initial sulfate reduction zone, but the success in identifying the magnetic polarity record down to 1,320 mbsf suggests that neither the repeated episodes of greigite authigenesis, nor the progressive conversion of greigite to pyrite and continued dissolution of magnetite, completely degraded the remanence record within the mud-rich sequence of Units I through V. Continuity of the polarity signal was only lost when the shift to the coarser, volcaniclastic-dominated lithology of Units VI and VII compounded the effects of progressive magnetic mineral diagenesis. Even within Units VI and VII some samples still record a stable remanence, evidenced by the recognition of reversed polarity in a few isolated samples (Musgrave & Kars, 2016). Stable remanence in these reduced, coarse-grained units may be carried by magnetite inclusions within silicates, as evidenced by the presence of a SD component in the sample from coarse-grained Unit VII (Figure 9D).

6. Conclusions

Site U1437 provides an 1,800-m-long record of magnetic mineral diagenesis in a setting with high geothermal gradient and low organic content relative to the detrital magnetic input, coupled with multiple fluid incursions driving episodes of late magnetic mineral diagenesis. Despite the impact of these fluid influxes, and the contrasting grain size between the mud-dominated upper 1,300 m and the coarser deeper part of the sequence, the sequence has a relatively simple background trend of progressive magnetic mineral diagenesis. Partial magnetite dissolution and greigite authigenesis, which began in the near-surface sulfidic zone but was repeatedly refreshed by later fluid incursions, was followed by slow reaction of the magnetic iron oxides and sulfides by prolonged exposure to low concentrations of pore water sulfide, which led to progressive conversion of greigite to pyrite and increasing dissolution of fine-grained magnetite. This progressive evolution of the magnetic mineralogy is best seen in the log-linear decrease in SIRM/κ with depth (and age), which despite the comparative complexity of the volcano-sedimentary basin sequence at Site U1437, resembles SIRM/κ profiles measured in lithologically monotonous hemipelagic sequences. The exponential decrease of SIRM/k with depth indicates that pyritization of greigite slows as burial depth and time increase, but continues to depths far below the SMT. Thermal instability of greigite, the mechanism suggested by Aubourg et al. (2012) for the loss of greigite with increasing burial, appears to be less important at Site U1437 than the continued reduction of greigite to pyrite. Continued pyritization requires a continuing, if small, supply of S^{2-} to depths which at U1437 exceed 1,500 mbsf.

Although the pattern of punctuated diagenetic responses to fluid inputs at Site U1437 is complex, some generalizations can be made. Influxes of water enriched in sulfate deep below the near-surface sulfate reduction zone resulted in renewed greigite authigenesis. Influx of methane and ethane also drove greigite formation in response to AOM in a mix of SD and SP size ranges. Some concentrations of methane in porous intervals are admixed with H_2S, resulting in the apparently contrary loss of greigite through reduction to pyrite.

The net result of both progressive and punctuated magnetic mineral diagenesis at Site U1437 is a protracted and repeated sequence of modifications of the magnetic mineralogy. Progressive diagenesis eventually degrades the remanence record to the point where magnetostratigraphy cannot be recognized, and punctuated diagenetic intervals appear to be responsible for a number of spurious polarity signals, including “ghost polarity intervals,” which lag the depositional record by tens of meters, but neither process overwhelmed the magnetostratigraphic record, which extends for over 1,300 m and has been confirmed by both paleontological and radiometric data. Where organic input is low, and detrital magnetite includes particles in the vortex to MD range or SD inclusions within silicates, even protracted and repeated late magnetic mineral diagenesis will not destroy the depositional remanence.

Acknowledgments
We acknowledge the contributions of all shipboard scientists of Expedition 350, whose work provides the foundations on which this study was constructed. We thank paleomagnetic technician Beth Novak and all the expedition technicians for their assistance. Andrew Roberts, David Heslop, and Xiang Zhao, Australian National University, provided access and assistance at the Black Mountain laboratory. The Institute for Rock Magnetism, University of Minnesota, provided access to their laboratory, and Mike Jackson and Peat Solheid offered technical advice and assistance. Mark Dekkers provided helpful comments on a draft of this paper. This research used samples and data provided by the International Ocean Discovery Program (IODP). Cruise participation and postcruise research by R. J. M. were supported financially by the Australia-New Zealand IODP Consortium. Postcruise research funding for M. K. was provided by JAMSTEC. R. J. M. and M. E. V. publish with the permission of the Executive Director, Geological Survey of New South Wales. Rock-magnetic data presented in the paper are available at https://nova.newcastle.edu.au/vital/access/manager/Repository. Shipboard pore water and headspace hydrocarbon data and the Expedition 350 Proceedings are available from the International Ocean Discovery Program, http://publications.iodp.org/proceedings/350/350title.html.

References

Aubourg, C., & Pozzi, J. P. (2010). Toward a new <250°C pyrrhotite-magnetite geothermometer for claystones. *Earth and Planetary Science Letters*, *294*(1-2), 47–57. https://doi.org/10.1016/j.epsl.2010.02.045

Aubourg, C., Pozzi, J.-P., & Kars, M. (2012). Burial, claystones remagnetization and some consequences for magnetostratigraphy. In R. D. Elmore, A. R. Muxworthy, M. M. Aldana, & M. Mena (Eds.), *Remagnetization and Chemical Alteration of Sedimentary Rocks*, *Special Publications* (Vol. 371, pp. 181–188). London: Geological Society. https://doi.org/10.1144/SP371.4

Banerjee, S. K., Hunt, C. P., & Liu, X.-M. (1993). Separation of local signals from the regional paleomonsoon record of the Chinese loess plateau: A rock-magnetic approach. *Geophysical Research Letters*, *20*(9), 843–846. https://doi.org/10.1029/93GL00908

Bloemendal, J., King, J. W., Hall, F. R., & Doh, S.-J. (1992). Rock magnetism of late Neogene and Pleistocene deep-sea sediments: Relationship to sediment source, diagenetic processes, and sediment lithology. *Journal of Geophysical Research*, *96*, 4361–4375.

Bottrell, S. H., Parkes, R. J., Cragg, B. A., & Raiswell, R. (2000). Isotopic evidence for deep anoxic pyrite oxidation and stimulation of bacterial sulfate reduction. *Journal of the Geological Society of London*, *157*(4), 711–714. https://doi.org/10.1144/jgs.157.4.711

Bowles, J., Jackson, M., & Banerjee, S. K. (2010). Interpretation of low-temperature data part II: The hematite Morin transition. *IRM Quarterly*, *20*(1), 1–10.

Brachfeld, S. A., Banerjee, S. K., Guyodo, Y., & Acton, G. D. (2002). A 13 200 year history of century to millennial-scale paleoenvironmental change magnetically recorded in the Palmer Deep, western Antarctic Peninsula. *Earth and Planetary Science Letters*, *194*(3-4), 311–326. https://doi.org/10.1016/S0012-821X(01)00567-2

Busby, C. J., Tamura, Y., Blum, P., Guèrin, G., Andrews, G. D. M., Barker, A. K., et al. (2017). The missing half of the subduction factory: Shipboard results from the Izu rear arc, IODP Expedition 350. *International Geology Review*, *59*(13), 1677–1708. https://doi.org/10.1080/00206814.2017.1292469

Canfield, D. E., & Thamdrup, B. (2009). Towards a consistent classification scheme for geochemical environments, or, why we wish the term 'suboxic' would go away. *Geobiology*, *7*(4), 385–392. https://doi.org/10.1111/j.1472-4669.2009.00214.x

Carter-Stiglitz, B., Moskowitz, B., Solheid, P., Berquó, T. S., Jackson, M., & Kosterov, A. (2006). Low-temperature magnetic behavior of multidomain titanomagnetites: TM0, TM16, and TM35. *Journal of Geophysical Research*, *111*, B12S05. https://doi.org/10.1029/2006JB004561

Chang, L., Heslop, D., Roberts, A. P., Rey, D., & Mohamed, K. J. (2016). Discrimination of biogenic and detrital magnetite through a double Verwey transition temperature. *Journal of Geophysical Research: Solid Earth*, *121*, 3–14. https://doi.org/10.1002/2015JB012485

Chang, L., Roberts, A. P., Heslop, D., Hayashida, A., Li, J., Zhao, X., et al. (2016). Widespread occurrence of silicate-hosted magnetic mineral inclusions in marine sediments and their contribution to paleomagnetic recording. *Journal of Geophysical Research: Solid Earth*, *121*, 8415–8431. https://doi.org/10.1002/2016JB013109

Chang, L., Roberts, A. P., Rowan, C. J., Tang, Y., Pruner, P., Chen, Q., & Horng, C. S. (2009). Low-temperature magnetic properties of greigite (Fe_3S_4). *Geochemistry, Geophysics, Geosystems*, *10*, Q01Y04. https://doi.org/10.1029/2008GC002276

Chang, L., Winklhofer, M., Roberts, A. P., Heslop, D., Florindo, F., Dekkers, M. J., et al. (2013). Low-temperature magnetic properties of pelagic carbonates: Oxidation of biogenic magnetite and identification of magnetosome chains. *Journal of Geophysical Research: Solid Earth*, *118*, 6049–6065. https://doi.org/10.1002/2013JB010381

Channell, J. E. T., & Hawthorne, T. (1990). Progressive dissolution of titanomagnetites at ODP Site 653 (Tyrrhenian Sea). *Earth and Planetary Science Letters*, *96*(3-4), 469–480. https://doi.org/10.1016/0012-821X(90)90021-O

Channell, J. E. T., & Xuan, C. (2009). Self-reversal and apparent magnetic excursions in Arctic sediments. *Earth and Planetary Science Letters*, *284*(1-2), 124–131. https://doi.org/10.1016/j.epsl.2009.04.020

Day, R., Fuller, M., & Schmidt, V. A. (1977). Hysteresis properties of titanomagnetites: Grain size and composition dependence. *Physics of the Earth and Planetary Interiors*, *13*(4), 260–267. https://doi.org/10.1016/0031-9201(77)90108-x

Dekkers, M. J., Langereis, C. C., Vriend, S. P., van Santvoort, P. J. M., & de Lange, G. J. (1994). Fuzzy c-means cluster analysis of early diagenetic effects on natural remanent magnetization acquisition in a 1.1 Myr piston core from the central Mediterranean. *Physics of the Earth and Planetary Interiors*, *85*(1-2), 155–171. https://doi.org/10.1016/0031-9201(94)90014-0

Dekkers, M. J., Mattéi, J.-L., Fillion, G., & Rochette, P. (1989). Grain-size dependence of the magnetic behaviour of pyrrhotite during its low-temperature transition at 34 K. *Geophysical Research Letters*, *16*(8), 855–858. https://doi.org/10.1029/GL016i008p00855

Dunlop, D. J. (2002a). Theory and application of the Day plot (M_{rs}/M_s versus H_{cr}/H_c) 1. Theoretical curves and tests using titanomagnetite data. *Journal of Geophysical Research*, *107*(B3), 2056. https://doi.org/10.1029/2001JB000486

Dunlop, D. J. (2002b). Theory and application of the Day plot (M_{rs}/M_s versus H_{cr}/H_c) 2. Application to data for rocks, sediments, and soils. *Journal of Geophysical Research*, *107*(B3), 2057. https://doi.org/10.1029/2001JB000487

Egli, R., Chen, A. P., Winklhofer, M., Kodama, K. P., & Horng, C.-S. (2010). Detection of noninteracting single domain particles using first-order reversal curve diagrams. *Geochemistry, Geophysics, Geosystems*, *11*, Q01Z11. https://doi.org/10.1029/2009GC002916

Expedition 334 Scientists (2012). Site U1381. In P. Vannuchi, K. Ujiie, N. Stroncik, A. Malinverno, & the Expedition 334 Scientists (Eds.), *Proceedings of the International Ocean Drilling Program*, 334. Tokyo: Integrated Ocean Drilling Program Management International, Inc. https://doi.org/10.2204/iodp.proc.334.106.2012

Frank, U., Nowaczyk, N. R., & Negendank, J. F. W. (2007). Rock magnetism of greigite bearing sediments from the Dead Sea, Israel. *Geophysical Journal International*, *168*(3), 921–934. https://doi.org/10.1111/j.1365-246X.2006.03273.x

Garming, J. F. L., Bleil, U., & Riedinger, N. (2005). Alteration of magnetic mineralogy at the sulfate-methane transition: Analysis of sediments from the Argentine continental slope. *Physics of the Earth and Planetary Interiors*, *151*(3-4), 290–308. https://doi.org/10.1016/j.pepi.2005.04.001

Gill, J. B., Bongiolo, E. M., Miyazaki, T., Hamelin, C., Jutzeler, M., DeBari, S., et al. (2018). Tuffaceous mud is a volumetrically important volcaniclastic facies of submarine arc volcanism and record of climate change. *Geochemistry, Geophysics, Geosystems*, *19*, 1217–1243. https://doi.org/10.1002/2017GC007300

Goldhaber, M. B. (2003). Sulfur-rich sediments. In F. T. Mackenzie (Ed.), Sediments, diagenesis, and sedimentary rocks. *Treatise on Geochemistry*, *7*, 257–288.

Halgedahl, S. L., & Jarrard, R. D. (1995). Low-temperature behavior of single-domain through multidomain magnetite. *Earth and Planetary Science Letters*, *130*(1-4), 127–139. https://doi.org/10.1016/0012-821X(94)00260-6

Harrison, R. J., & Feinberg, J. M. (2008). FORCinel: An improved algorithm for calculating first-order reversal curve distributions using locally weighted regression smoothing. *Geochemistry, Geophysics, Geosystems*, *9*, Q05016. https://doi.org/10.1029/2008GC001987

Heslop, D., Roberts, A. P., & Chang, L. (2014). Characterizing magnetofossils from first-order reversal curve (FORC) central ridge signatures. *Geochemistry, Geophysics, Geosystems*, *15*, 2170–2179. https://doi.org/10.1002/2014GC005291

Horng, C.-S., & Chen, K.-H. (2006). Complicated magnetic mineral assemblages in marine sediments offshore of southwestern Taiwan: Possible influence of methane flux on the early diagenetic process. *Terrestrial, Atmospheric and Oceanic Sciences*, *17*, 109–1026.

Horng, C.-S., & Roberts, A. P. (2018). The low-temperature Besnus magnetic transition: Signals due to monoclinic and hexagonal pyrrhotite. *Geochemistry, Geophysics, Geosystems*, *19*, 3364–3375. https://doi.org/10.1029/2017GC007394

Housen, B. A., & Musgrave, R. J. (1996). Rock-magnetic signature of gas hydrates in accretionary prism sediments. *Earth and Planetary Science Letters*, *139*(3-4), 509–519. https://doi.org/10.1016/0012-821X(95)00245-8

Jackson, M., & Swanson-Hysell, N. L. (2012). Rock magnetism of remagnetized carbonate rocks: Another look. *Geological Society, London, Special Publications*, *371*(1), 229–251. https://doi.org/10.1144/SP371.3

Jiang, W.-T., Horng, C.-S., Roberts, A. P., & Peacor, D. R. (2001). Contradictory magnetic polarities in sediments and variable timing of neoformation of authigenic greigite. *Earth and Planetary Science Letters*, *193*(1-2), 1–12. https://doi.org/10.1016/S0012-821X(01)00497-6

Jørgensen, B. B., Böttcher, M. E., Lüschen, H., Neretin, L. N., & Volkov, I. I. (2004). Anaerobic methane oxidation and a deep H_2S sink generate isotopically heavy sulfides in Black Sea sediments. *Geochimica et Cosmochimica Acta*, *68*(9), 2095–2118. https://doi.org/10.1016/j.gca.2003.07.017

Jørgensen, B. B., & Kasten, S. (2006). Sulfur cycling and methane oxidation. In H. D. Schulz & M. Zabel (Eds.), *Marine Geochemistry* (pp. 271–309). Berlin: Springer. https://doi.org/10.1007/3-540-32144-6_8

Kars, M., Aubourg, C., Labaume, P., Berquó, T. S., & Cavailhes, T. (2014). Burial diagenesis of magnetic minerals: New insights from the Grès D'Annot transect (SE France). *Minerals*, *4*(3), 667–689. https://doi.org/10.3390/min4030667

Kars, M., Aubourg, C., Pozzi, J.-P., & Janots, D. (2012). Continuous production of nanosized magnetite through low grade burial. *Geochemistry, Geophysics, Geosystems*, *13*, Q08Z48. https://doi.org/10.1029/2012GC004104

Kars, M., & Kodama, K. (2015). Authigenesis of magnetic minerals in gas hydrate-bearing sediments in the Nankai Trough, offshore Japan. *Geochemistry, Geophysics, Geosystems*, *16*, 947–961. https://doi.org/10.1002/2014GC005614

Kars, M., Musgrave, R. J., Hoshino, T., Jonas, A.-S., Bauersachs, T., Inagaki, F., & Kodama, K. (2018). Magnetic mineral diagenesis in a high temperature and deep methanic zone in Izu rear arc marine sediments, northwest Pacific Ocean. *Journal of Geophysical Research: Solid Earth*, *123*, 8331–8348. https://doi.org/10.1029/2018JB015861

Kars, M., Musgrave, R. J., Kodama, K., Jonas, A.-S., Bordiga, M., Ruebsam, W., et al. (2017). Impact of climate change on the magnetic mineral assemblage in marine sediments from Izu rear arc, NW Pacific Ocean, over the last 1 Myr. *Palaeogeography, Palaeoclimatology, Palaeoecology*, *480*, 53–69. https://doi.org/10.1016/j.palaeo.2017.05.016

Kasten, S., Freudenthal, T., Gingele, F. X., & Schulz, H. D. (1998). Simultaneous formation of iron-rich layers at different redox boundaries in sediments of the Amazon deep-sea fan. *Geochimica et Cosmochimica Acta*, *62*(13), 2253–2264. https://doi.org/10.1016/S0016-7037(98)00093-3

Kawamura, N., Ishikawa, N., & Torii, M. (2012). Diagenetic alteration of magnetic minerals in Labrador Sea sediments (IODP Sites U1305, U1306, and U1307). *Geochemistry, Geophysics, Geosystems*, *13*, Q08013. https://doi.org/10.1029/2012GC004213

Kruiver, P. P., & Passier, H. F. (2001). Coercivity analysis of magnetite phases in sapropel S1 related to variations in redox conditions, including investigation of the S-ratio. *Geochemistry, Geophysics, Geosystems*, *2*. https://doi.org/10.1029/2001GC000181

Larrasoaña, J. C., Roberts, A. P., Musgrave, R. J., Gràcia, E., Piñero, E., Vega, M., & Martínez-Ruiz, F. (2007). Diagenetic formation of greigite and pyrrhotite in gas hydrate marine sedimentary systems. *Earth and Planetary Science Letters*, *123*(9), 7285–7304. https://doi.org/10.1029/2018JB015909

Larrasoaña, J. C., Roberts, A. P., Stoner, J. S., Richter, C., & Wehausen, R. (2003). A new proxy for bottom-water ventilation in the eastern Mediterranean based on diagenetically controlled magnetic properties of sapropel-bearing sediments. *Palaeogeography, Palaeoclimatology, Palaeoecology*, *190*, 221–242. https://doi.org/10.1016/S0031-0182(02)00607-7

Lascu, I., Einsle, J. F., Ball, M. R., & Harrison, R. J. (2018). The vortex state in geologic materials: a micromagnetic perspective. *Journal of Geophysical Research: Solid Earth*, *123*, 7285–7304. https://doi.org/10.1029/2018JB015909

Mleneck-Vautravers, M. J. (2018). Quantitative planktonic foraminifers taphonomy and palaeoceanographic implications over the last 1 My from IODP Sites U1436 and U1437. *Cogent Geoscience*, *4*(1), 1447263. https://doi.org/10.1080/23312041.2018.1447263

Morin, F. J. (1950). Magnetic susceptibility of α-Fe_2O_3 and α-Fe_2O_3 with added titanium. *Physical Review*, *78*(6), 819–820. https://doi.org/10.1103/PhysRev.78.819.2

Moskowitz, B. M., Frankel, R. B., & Bazylinski, D. A. (1993). Rock magnetic criteria for the detection of biogenic magnetite. *Earth and Planetary Science Letters*, *120*(3-4), 283–300. https://doi.org/10.1016/0012-821X(93)90245-5

Moskowitz, B. M., Jackson, M., & Kissel, C. (1998). Low-temperature magnetic behavior of titanomagnetites. *Earth and Planetary Science Letters*, *157*(3-4), 141–149. https://doi.org/10.1016/S0012-821X(98)00033-8

Musgrave, R. J., Bangs, N. L., Larrasoaña, J. C., Gràcia, E., Hollamby, J. A., & Vega, M. E. (2006). Rise of the base of the gas hydrate zone since the last glacial recorded by rock magnetism. *Geology*, *34*(2), 117–120. https://doi.org/10.1130/G22008.1

Musgrave, R. J., Collombat, H., & Didenko, A. N. (1995). Magnetic sulfide diagenesis, thermal overprinting, and paleomagnetism of accretionary wedge and convergent margin sediments from the Chile Triple Junction region. *Proceeding of the Ocean Drilling Program, Scientific Results*, *141*, 59–78.

Musgrave, R. J., Delaney, M. L., Stax, R., & Tarduno, J. A. (1993). Magnetic diagenesis, organic input, interstitial water chemistry, and paleomagnetic record of the carbonate sequence on the Ontong Java Plateau. *Proceeding of the Ocean Drilling Program, Scientific Results*, *130*, 527–546.

Musgrave, R. J., & Kars, M. (2016). Recognizing magnetostratigraphy in overprinted and altered marine sediments: Challenges and solutions from IODP Site U1437. *Geochemistry, Geophysics, Geosystems*, *17*, 3190–3206. https://doi.org/10.1002/2016GC006386

Muxworthy, A. R., & McClelland, E. (2000). Review of the low-temperature magnetic properties of magnetite from a rock magnetic perspective. *Geophysical Journal International*, *140*(1), 101–114. https://doi.org/10.1046/j.1365-246x.2000.00999.x

Neretin, L. N., Böttcher, M. E., Jørgensen, B. B., Volkov, I. I., Lüschen, H., & Hilgenfeldt, K. (2004). Pyritization processes and greigite formation in the advancing sulfidization front in the Upper Pleistocene sediments of the Black Sea. *Geochimica et Cosmochimica Acta*, *68*(9), 2081–2093. https://doi.org/10.1016/S0016-7037(03)00450-2

Özdemir, Ö., & Dunlop, D. J. (2010). Hallmarks of maghemitization in low-temperature remanence cycling of partially oxidized magnetite nanoparticles. *Journal of Geophysical Research*, *115*, B02101. https://doi.org/10.1029/2009JB006756

Özdemir, Ö., Dunlop, D. J., & Berquó, T. S. (2008). Morin transition in hematite: Size dependence and thermal hysteresis. *Geochemistry, Geophysics, Geosystems*, *9*, Q10Z01. https://doi.org/10.1029/2008GC002110

Özdemir, Ö., Dunlop, D. J., & Moskowitz, B. M. (1993). The effect of oxidation on the Verwey transition in magnetite. *Geophysical Research Letters*, *20*(16), 1671–1674. https://doi.org/10.1029/93GL01483

Passier, H. F., & Dekkers, M. J. (2002). Iron oxide formation in the active oxidation front above sapropel S1 in the eastern Mediterranean Sea as derived from low-temperature magnetism. *Geophysical Journal International*, *150*(1), 230–240. https://doi.org/10.1046/j.1365-246X.2002.01704.x

Pike, C. R., Roberts, A. P., & Verosub, K. L. (1999). Characterizing interactions in fine magnetic particle systems using first order reversal curves. *Journal of Applied Physics*, *85*(9), 6660–6667. https://doi.org/10.1063/1.370176

Reynolds, R. L., Tuttle, M. L., Rice, C. A., Fishman, N. S., Karachewski, J. A., & Sherman, D. M. (1994). Magnetization and geochemistry of greigite-bearing Cretaceous strata, North Slope basin, Alaska. *American Journal of Science*, *294*(4), 485–528. https://doi.org/10.2475/ajs.294.4.485

Roberts, A. P. (1995). Magnetic characteristics of sedimentary greigite (Fe_3S_4). *Earth and Planetary Science Letters*, *134*(3-4), 227–236. https://doi.org/10.1016/0012-821X(95)00131-U

Roberts, A. P. (2015). Magnetic mineral diagenesis. *Earth-Science Reviews*, *151*, 1–47. https://doi.org/10.1016/j.earscirev.2015.09.010

Roberts, A. P., Almeida, T. P., Church, N. S., Harrison, R. J., Heslop, D., Li, Y. L., et al. (2017). Resolving the origin of pseudo-single domain magnetic behavior. *Journal of Geophysical Research: Solid Earth*, *122*, 9534–9558. https://doi.org/10.1002/2017JB014860

Roberts, A. P., Chang, L., Rowan, C. J., Horng, C. S., & Florindo, F. (2011). Magnetic properties of sedimentary greigite (Fe_3S_4): An update. *Reviews of Geophysics*, *49*, RG1002. https://doi.org/10.1029/2010rg000336.1

Roberts, A. P., Florindo, F., Larrasoaña, J. C., O'Regan, M. A., & Zhao, X. (2010). Complex polarity pattern at the (former) Plio-Pleistocene global stratotype section at Vrica (Italy): Remagnetization by magnetic iron sulphides. *Earth and Planetary Science Letters*, *292*(1-2), 98–111. https://doi.org/10.1016/j.epsl.2010.01.025

Roberts, A. P., Heslop, D., Zhao, X., & Pike, C. R. (2014). Understanding fine magnetic particle systems through use of first-order reversal curve diagrams. *Reviews of Geophysics*, *52*, 557–602. https://doi.org/10.1002/2014RG000462

Roberts, A. P., Pike, C. R., & Verosub, K. L. (2000). First-order reversal curve diagrams: A new tool for characterizing the magnetic properties of natural samples. *Journal of Geophysical Research*, *105*(B12), 28461–28475. https://doi.org/10.1029/2000JB900326

Roberts, A. P., Tauxe, L., Heslop, D., Zhao, X., & Jiang, Z. (2018). A critical appraisal of the "Day" diagram. *Journal of Geophysical Research: Solid Earth*, *123*, 2618–2644. https://doi.org/10.1002/2017JB015247

Roberts, A. P., & Weaver, R. (2005). Multiple mechanisms of remagnetization involving sedimentary greigite (Fe_3S_4). *Earth and Planetary Science Letters*, *231*(3-4), 263–277. https://doi.org/10.1016/j.epsl.2004.11.024

Rochette, P., Fillion, G., Mattéi, J.-L., & Dekkers, M. J. (1990). Magnetic transition at 30–34 K in pyrrhotite: Insight into a widespread occurrence of this mineral in rocks. *Earth and Planetary Science Letters*, *98*(3-4), 319–328. https://doi.org/10.1016/0012-821X(90)90034-U

Rowan, C. J., & Roberts, A. P. (2008). Widespread remagnetizations and a new view of Neogene tectonic rotations within the Australia-Pacific plate boundary zone, New Zealand. *Journal of Geophysical Research*, *113*, B03103. https://doi.org/10.1029/2006JB004594

Rowan, C. J., Roberts, A. P., & Broadbent, T. (2009). Reductive diagenesis, magnetite dissolution, greigite growth and paleomagnetic smoothing in marine sediments: A new view. *Earth and Planetary Science Letters*, *277*(1-2), 223–235. https://doi.org/10.1016/j.epsl.2008.10.016

Sagnotti, L., Roberts, A. P., Weaver, R., Verosub, K. L., Florindo, F., Pike, C. R., et al. (2005). Apparent magnetic polarity reversals due to remagnetization resulting from late diagenetic growth of greigite from siderite. *Geophysical Journal International*, *160*(1), 89–100. https://doi.org/10.1111/j.1365-246X.2005.02485.x

Schmitt, A. K., Konrad, K., Andrews, G. D. M., Horie, K., Brown, S. R., Koppers, A. A. P., et al. (2017). $^{40}Ar/^{39}Ar$ ages and zircon petrochronology for the rear arc of the Izu–Bonin–Marianas intra-oceanic subduction zone. *International Geology Review*, *60*(8), 956–976. https://doi.org/10.1080/00206814.2017.1363675

Shi, M., Wu, H., Roberts, A. P., Zhang, S., Zhao, X., Li, H., et al. (2017). Tectonic, climatic, and diagenetic control of magnetic properties of sediments from Kumano Basin, Nankai margin, southwestern Japan. *Marine Geology*, *391*, 1–12. https://doi.org/10.1016/j.margeo.2017.07.006

Shipboard Scientific Party (1994). Sites 889 and 890. In G. K. Westbrook, et al. (Eds.), *Proceedings of the Ocean Drilling Program, Initial Reports (Pt. 1)* (Vol. 146-1, pp. 127–329). College Station, TX: Ocean Drilling Program. https://doi.org/10.2973/odp.proc.ir.146-1.008.1994

Shipboard Scientific Party (1996a). Site 994. In C. K. Paul, et al. (Eds.), *Proceedings of the Ocean Drilling Program, Initial Reports* (Vol. 164, pp. 99–174). College Station, TX: Ocean Drilling Program. https://doi.org/10.2973/odp.proc.ir.164.107.1996

Shipboard Scientific Party (1996b). Site 997. In C. K. Paul, et al. (Eds.), *Proceedings of the Ocean Drilling Program, Initial Reports* (pp. 164, 277–334). College Station, TX: Ocean Drilling Program. https://doi.org/10.2973/10.2973/odp.proc.ir.164.110.1996

Shipboard Scientific Party (1997). Site 1039. In G. Kimura, E. Silver, P. Blum, et al. (Eds.), *Proceedings of the Ocean Drilling Program, Initial Reports* (Vol. 170, pp. 45–93). College Station, TX: Ocean Drilling Program. https://doi.org/10.2973/odp.proc.ir.170.103.1997

Snowball, I. F. (1991). Magnetic hysteresis properties of greigite (Fe_3S_4) and a new occurrence in Holocene sediments from Swedish Lappland. *Physics of the Earth and Planetary Interiors*, *68*(1-2), 32–40. https://doi.org/10.1016/0031-9201(91)90004-2

Tamura, Y., Busby, C. J., Blum, P., Guèrin, G., Andrews, G. D. M., Barker, A. K., et al. (2015). Site U1437. In Y. Tamura, C. J. Busby, P. Blum, & the Expedition 350 Scientists (Eds.), *Proceedings of the International Ocean Discovery Program, Expedition 350: Izu-Bonin-Mariana Rear Arc* (pp. 1–142). College Station, TX: International Ocean Discovery Program. https://doi.org/10.14379/iodp.proc.350.104.2015

Tarduno, J. A. (1992). Magnetic susceptibility cyclicity and magnetite dissolution in Cretaceous limestones of the southern Alps (Italy). *Geophysical Research Letters*, *19*(14), 1515–1518. https://doi.org/10.1029/92GL01484

van Dongen, B. E., Roberts, A. P., Schouten, S., Jiang, W.-T., Florindo, F., & Pancost, R. D. (2007). Formation of iron sulfide nodules during anaerobic oxidation of methane. *Geochimica et Cosmochimica Acta*, *71*, 5155–5167. https://doi.org/10.1016/j.gca.2007.08.019

Verwey, E. J. W. (1939). Electronic conduction of magnetite (Fe_3O_4) and its transition point at low temperatures. *Nature*, *144*(3642), 327–328. https://doi.org/10.1038/144327b0

Weaver, R., Roberts, A. P., & Barker, A. J. (2002). A late diagenetic (synfolding) magnetization carried by pyrrhotite: Implications for paleomagnetic studies from magnetic iron sulphide-bearing sediments. *Earth and Planetary Science Letters*, *200*(3-4), 371–386. https://doi.org/10.1016/S0012-821X(02)00652-0